

Air Phase Entrapment Role in Hydrophobic Particle-Water-Air Mixtures Internal Structure and Density

Wenpei Ma¹ and Ingrid Tomac¹

¹University of California San Diego

April 11, 2024

Abstract

Post-wildfire mudflows, in which more than half of the solids are sand or smaller, destroy the watershed environment, life, and infrastructures. The surficial soil particles turn hydrophobic due to the deposition of combusted organic matter during wildfires. Initiated by raindrops splash, runoff and erosion grow into devastating mudflows, quickly blasting obstacles on the way, and carrying large boulders and debris. The internal composition of post-wildfire mudflows has recently become of interest, intending to understand better mechanisms and transport differences between post-wildfire mudflows and non-post-wildfire mudflows. This paper shows critical new insights into how the air got entrapped during the early stage of mudflow and how air entrapment affects the properties of post-wildfire mudflows as a mixture of air bubbles, water, and hydrophobic sand. This paper proposes and experimentally investigates a new paradigm in which a significant amount of air remains entrapped in post-wildfire mudflow via hydrophobic-particle-air attraction. The mudflow mixture's internal structure depends on the physical state of small liquid marbles, which are small air bubbles covered by hydrophobic sand particles. This paper quantifies the amount of air trapped under different sand-water volumetric concentrations, the effects of mixing speeds (energy), mixing duration, and sand particle size on the final mudflow internal structure. In addition, this paper proposes an empirical estimation of density reductions due to air entrapment in the mixture during the mixing process.

Hosted file

Paper1_WRR_r0.docx available at <https://authorea.com/users/533185/articles/742324-air-phase-entrapment-role-in-hydrophobic-particle-water-air-mixtures-internal-structure-and-density>

Hosted file

Supporting Information_V1.docx available at <https://authorea.com/users/533185/articles/742324-air-phase-entrapment-role-in-hydrophobic-particle-water-air-mixtures-internal-structure-and-density>

1 **Air Phase Entrapment Role in Hydrophobic Particle-Water-Air Mixtures Internal Structure and**
2 **Density**

3
4 **W. Ma¹ and I. Tomac¹**

5 ¹ University of California San Diego, Department of Structural Engineering, La Jolla 92093,
6 C.A.

7 Corresponding author: Ingrid Tomac (itomac@ucsd.edu)

8

9 **Key Points:**

- 10 • Post-wildfire mudflows contain hydrophobic particles affecting mixture composition and
11 density
- 12 • The strong attraction of hydrophobic particles to air bubbles in water leads to a
13 heterogeneous mixture with significant amounts of air.

14

15 **Abstract**

16 Post-wildfire mudflows, in which more than half of the solids are sand or smaller, destroy the
17 watershed environment, life, and infrastructures. The surficial soil particles turn hydrophobic due
18 to the deposition of combusted organic matter during wildfires. Initiated by raindrops splash,
19 runoff and erosion grow into devastating mudflows, quickly blasting obstacles on the way, and
20 carrying large boulders and debris. The internal composition of post-wildfire mudflows has
21 recently become of interest, intending to understand better mechanisms and transport differences
22 between post-wildfire mudflows and non-post-wildfire mudflows. This paper shows critical new
23 insights into how the air got entrapped during the early stage of mudflow and how air entrapment
24 affects the properties of post-wildfire mudflows as a mixture of air bubbles, water, and
25 hydrophobic sand. This paper proposes and experimentally investigates a new paradigm in which
26 a significant amount of air remains entrapped in post-wildfire mudflow via hydrophobic-particle-
27 air attraction. The mudflow mixture's internal structure depends on the physical state of small
28 liquid marbles, which are small air bubbles covered by hydrophobic sand particles. This paper
29 quantifies the amount of air trapped under different sand-water volumetric concentrations, the
30 effects of mixing speeds (energy), mixing duration, and sand particle size on the final mudflow
31 internal structure. In addition, this paper proposes an empirical estimation of density reductions
32 due to air entrapment in the mixture during the mixing process.

33

34 **1 Introduction**

35 Post-wildfire mudflows are devastating natural disasters whose frequency increases with climate
36 change and wildfire events worldwide, including California and the Western US, Pacific West,
37 Canada, Europe, and the Mediterranean. In addition, the severity of fire events is likely to
38 increase in the future for most areas due to an increase in regional temperature and dryness

39 (Fried et al., 2004; Westerling & Bryant, 2008; Westerling et al., 2011; Abatzoglou & Williams,
40 2016; Lozano et al., 2017; Wotton et al., 2017; Williams et al., 2019; Dupuy et al., 2020; Goss et
41 al., 2020; Halofsky et al., 2020). Post-wildfire mud- and debris flow differ from most natural
42 mudflows because of fire-induced soil wettability modifications. Wildfires combust organic fuel
43 like plant parts in soil and generate hydrophobic substances that precipitate and coat granular soil
44 particles (DeBano et al., 1979; DeBano, 1981, 1991, 2000a; Neary et al., 2005). The fire-induced
45 hydrophobic soil layer averages between 6 cm and 16 cm reported on burned chaparral lands in
46 southern California in the 1960s (DeBano et al., 1967; Savage, 1974; DeBano et al., 1976;
47 DeBano, 2000a, 2000b; Neary et al., 2005), and has been regularly classified in Burned Area
48 Response (BAER) reports (USDA Forest Service, 2021a, 2021b, 2021c). According to Morell et
49 al. (2021), the 2018 Montecito debris flow eroded at least 550,000 m³ of sediment, and scour
50 depth was between 0.5 m to 2 m. Therefore, assuming the entire layer of fire-induced
51 hydrophobic soil has been eroded during the flood, a rough estimate is that 3% to 32% of
52 Montecito sediments contain hydrophobic soils. Considering the time factor of the flooding
53 process, this percentage must be higher at the beginning of an erosion event. Although wildfires
54 can also reduce the long-term soil hydrophobicity in rare, naturally highly water-repellent areas
55 (Tessler et al., 2013), this research applies to regions with naturally wettable soil that becomes
56 hydrophobic after wildfire, like the USA's arid southwest.

57 Post-fire mudflows initiate as shallow slopes when rain erodes burned scars' loose
58 surficial soil layers and subsequently carry debris downhill, endangering lives and properties
59 (Cannon et al., 2001; Cannon et al., 2008; Kean et al., 2019). The field's internal structure and
60 composition of post-wildfire mudflows are difficult to quantify due to their short duration and
61 fast flows, up to 30 km/h (Cui et al., 2018). Limited studies have reported post-wildfire sediment
62 yield, hydraulic recovery, hydrophobic bed role, entrainment into mudflows, and erosion patterns

63 (Kean et al., 2011; Lamb et al., 2011; Ng et al., 2022; Perkins et al., 2022). For example, the
64 solid volumetric concentration varies and can be as high as 60 % in post-wildfire mudflows and
65 debris flows (Conedera et al., 2003; Cannon et al., 2001; Cannon et al., 2008; Kean et al., 2011;
66 Cui et al., 2018; Lee & Widjaja, 2013). In addition to solids and water, Bull (1963) described for
67 the first time how air entrapment occurs in mudflows. Mudflow traps air from the atmosphere
68 while flowing down the tributary ravines and channels, and existing air from pores in the soil
69 deposits can roll into the mudflow. Bull (1963) postulated that part of the air becomes trapped by
70 mudflow and forms bubble cavities that are qualitatively shown in mudflow deposit images and
71 have different shapes and sizes based on sediment material. Furthermore, mudflows can entrap
72 air when obstacles impact the flow (Song et al., 2021; Garoosi et al., 2022). In addition, the air
73 entrapment rate in a granular flow depends on the gradient of solid velocity and flow thickness
74 (Sheng et al., 2013), enhanced by particle hydrophobicity (Cervantes-Álvarez et al., 2020).

75 Since wildfires turn surficial soil hydrophobic and dried contents of post-fire mudflows
76 likely contain excess air, this paper investigates micromechanics of hydrophobic particle-air-
77 water mixtures to understand better post-wildfire internal composition, air entrapment
78 mechanisms, and density modifications. While previous research highlighted the importance of
79 solids availability on total air entrapment when grains enter the water, further enhanced by
80 hydrophobicity (Cervantes-Álvarez et al., 2020; Ong et al., 2021), the air entrapment dynamics
81 has not been fully quantified for flowing mixtures. Wang et al. (2016) observed submerged three
82 particle-air bubble detachment mechanisms: centrifugal force on particles due to the rotation of
83 the air bubble about its axis in a vortex, irregular trajectories of the particle-bubble complex
84 under motion, strong oscillation of the bubble surface which expels the particles. Furthermore,
85 although many studies investigate the formation and stability of a single liquid marble, which is
86 an air bubble whose surface is covered with a layer of hydrophobic particles (Bormaschenko,

87 2011; McHale and Newton, 2011, 2015), as further explained in the Supporting Information S1 –
88 S3, the macro-level effects of particle-bubble interactions and dynamics of liquid marbles
89 formation in a flowing mixture with numerous particles and bubbles are poorly understood.
90 Therefore, this paper aims to quantify experimentally and theoretically how kinetic energy,
91 mixing time, interphase forces and dynamics, phase ratios, and solid particles' physical
92 properties, like size, affect the amount of entrapped air via the liquid marble mechanism during
93 water-particle-air mixing. In addition to mudflows, air entrapment into particle-water slurries is
94 relevant in engineering applications (Suhr et al., 1984; Römkens et al., 1997; Sheng et al., 2013;
95 Tanaka et al., 2019; Cervantes-Álvarez et al., 2020; Dunkerley, 2020; Ong et al., 2021; Garoosi
96 et al., 2022).

97

98 **2 Methodology**

99 This research focuses on sand mixtures because wildfires do not alter hydrophobicity on
100 cohesive soils like clays but significantly affect sands and gravels in highly erodible areas
101 (Debano, 1981; Huffman et al., 2001). Although post-mudflow reconnaissance typically does not
102 quantify volumes of displaced hydrophobic soils, early-stage mudflows are composed of eroded
103 hydrophobic particles from burned scar surfaces. Specifically, this paper studies how air
104 entrapped by hydrophobic particles changes internal structure composition and density in
105 controlled laboratory conditions. Since previous research shows that laboratory sands can well
106 represent site soils following standard geotechnical procedures (Movasat & Tomac, 2021), this
107 research uses clean sand with small sieve sizes to better understand sand size's role in air
108 entrapment. Although post-mudflow reconnaissance efforts to date missed to identify volumes of
109 displaced hydrophobic soils, this study investigates the worst-case scenario and early-stage
110 mudflows as composed of eroded hydrophobic particles from burned scar surfaces.

111 Experiments consider three types of sand: sieved 10/16 coarse sand (mean particle
 112 diameter: 1.33 mm), sieved 40/50 medium silica sand (mean particle diameter: 0.27 mm), and
 113 American Foundry Society (AFS) 50/70 testing Ottawa silica fine sand (mean particle diameter:
 114 0.15 mm). Sand is mixed with blades in a 290-ml volume cup with an overall 75-mm height and
 115 a 70-mm diameter. After removing fine dust by washing, the sand is oven-dried for 24 hours at
 116 100 °C, and then submerged in a mixed solution of 10% Triethoxy-n-octylsilane (C₁₄H₃₂O₃Si)
 117 and 90% isopropyl alcohol by volume for at least 48 hours at room temperature, which builds a
 118 hydrophobic coating. After the treatment, hydrophobic sand is washed in water and oven dried.
 119 Table 1 summarizes the mean contact angles and water drop penetration times for each type of
 120 sand after hydrophobicity treatment and includes hydrophobic soil samples from the fire sites
 121 and hydrophilic (untreated) sand. Hydrophobicity classification uses the same method in Bisdom
 122 et al. (1993) and Leelamanie et al. (2008). The initial volumetric sand-to-water ratio is
 123 determined by measuring the sand weight and using the sand's specific gravity (G_s) to obtain the
 124 volume of sand solids. Specific gravity is the ratio of the sand grain density to the density of
 125 water. The specific gravity for fine, medium, and coarse sand is measured as 2.65, 2.65, and
 126 2.64, respectively.

127

128 **Table 1.** Mean Contact angles and water drop penetration times for different types of artificial
 129 hydrophobic sand, hydrophilic (untreated) sand, and hydrophobic sand from a fire site.

Sand Type	Mean Contact Angle, (°)	Water Drop Penetration Time (s) and Repellency Category
Hydrophobic Soil from Fire Site	112 ± 9.6	> 600 (severely water-repellent)
Artificial Hydrophobic Fine Sand	120 ± 8.1	> 3600 (extremely water-repellent)

Artificial Hydrophobic Medium Sand	112 ± 6.4	> 3600 (extremely water-repellent)
Artificial Hydrophobic Coarse Sand	109 ± 8.9	> 3600 (extremely water-repellent)
Hydrophilic (Normal) Fine Sand	57 ± 2.1	0.08 (Wettable / Non-repellent)
Hydrophilic (Normal) Medium Sand	70 ± 2.8	0.02 (Wettable / Non-repellent)
Hydrophilic (Normal) Coarse Sand	68 ± 3.5	0.02 (Wettable / Non-repellent)

130

131 A comprehensive mixing program is performed in controlled laboratory conditions to
132 investigate the extent and forms of entrapped air after mixing. The custom mixing system uses a
133 1-HP motor and variable-frequency drive (VFD) that controls the speed of the mixer blade.
134 Multi-purpose Synthetic Grease prevents all possible water or air leakages from gaps around the
135 container. Before mixing, a certain amount of sand sits at the bottom of the container, followed
136 by pouring water above the sand layer. Air exists naturally within the hydrophobic sand layer
137 and above the water layer within the container. Supporting Information S5 shows details of the
138 mixing blade and investigates the effect of mixing blade shape. Mixing in a cup and vane system
139 replicates kinetic energy and shear rates in post-wildfire mudflows. The shear rates in
140 approximately 1 m high mudflows, at 30 km/h (8.3 m/s) average mudflow velocity, produce
141 shear rates in the order of tens of s^{-1} in laminar regimes. Using the equivalent energy principle as
142 an alternative approach ensures mixing equivalence of the highly heterogeneous three-phase
143 mixture due to the flow regime and dynamics being erratic in nature due to changes of downhill
144 slopes, slope lengths, and natural obstacles, and thus to a large extent unknown before the
145 experiment. Therefore, the vane and cup mixing speed relates to a possible downhill mixture
146 velocity using the work-energy principle:

$$KE_{translational} = \frac{1}{2}mv^2 \quad (1)$$

147 where $KE_{translational}$ is the kinetic energy of the mixture mass at a translational motion; m is the
 148 mixture mass; and v is the linear velocity of the mixture during a mudflow event. Eqn. 2 defines
 149 the rotational kinetic energy in the experiments using the work-energy principle:

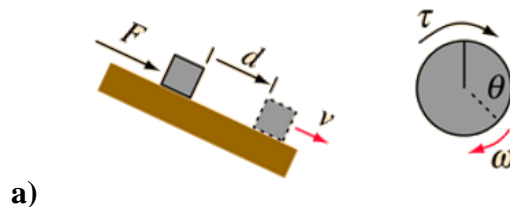
$$KE_{rotational} = \frac{1}{2}I\omega^2 \quad (2)$$

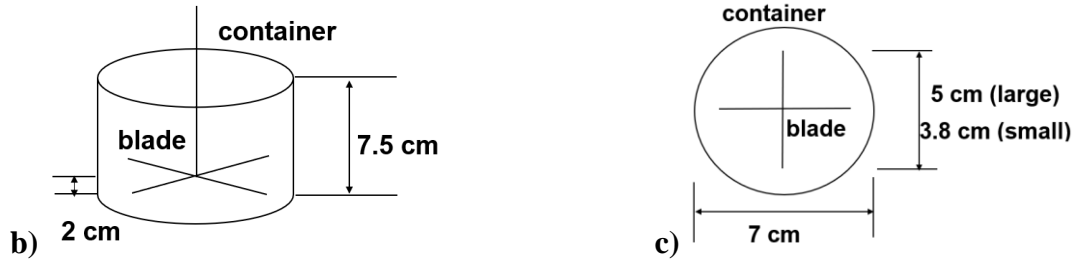
150 where $KE_{rotational}$ is the kinetic energy of the mixture mass at a rotational motion; ω is the
 151 angular velocity; and I is the moment of inertia of the mixture. When the mixing blade rotates,
 152 the mixture resembles a hollow cylinder shape with a thin boundary layer at the wall edge; thus, I
 153 is estimated for a cylindrical container shown in **Fig. 1**. By equating $KE_{translational}$ in Eqn. 1
 154 and $KE_{rotational}$ in Eqn. 2, one can easily obtain the relationship between translational velocity v
 155 from the field and angular velocity ω used in experiments as follows:

$$\omega = \sqrt{\frac{mv^2}{I}} \quad (3)$$

156 The following example demonstrates the calculation: a 30.5-g of fine sand and 218.5-g water
 157 mixture, rotating at an angular velocity of 314 rad/s, is subjected to a total rotational energy of
 158 3.84 kg-m²/s². However, when the same mixture mass is subjected to equivalent kinetic energy
 159 flowing downhill, it reaches the velocity of 5.6 m/s.

160





161 **Figure 1. a)** Relations between downhill velocity and experimental rotational agitation, **b)** Front
 162 view and the dimension of the mixing container, **c)** Top view and the dimension of the mixing
 163 container

164

165 Experiments vary fluid mixing speed, mixing time, and initial solid volumetric
 166 concentration of sand (V_s) to the water (V_w) across shear rates, and mixing time varies from 10 s
 167 to 120 s. Then, the mixing time increases until evident air-entrapment level changes cease.
 168 Depending on how many sand particles are available initially and the type of sand particles, the
 169 degas process ends at different times. The degassing process does not change significantly after
 170 60 s for fine sand and after 40 s for medium and coarse sand. The mixing duration stops at 120 s
 171 for fine sand, 80 s for medium sand, and 90 s for coarse sand. Before and after mixing, water
 172 surface levels help determine the volumes of free air, escaped air, free water, sand particles, and
 173 entrapped air. Image documentation of side and top views helps visualize the physical presence
 174 and sizes of liquid marbles and sediment.

175 This paper introduces the specific air content (e^*), the main parameter describing how
 176 much air gets entrapped during the mixing process. It is the ratio between the total volume of
 177 entrapped air (V_a) to the volume of initial sand particles (V_s):

$$e^* = \frac{V_a}{V_s} \quad (4)$$

178

179 **3 Results**

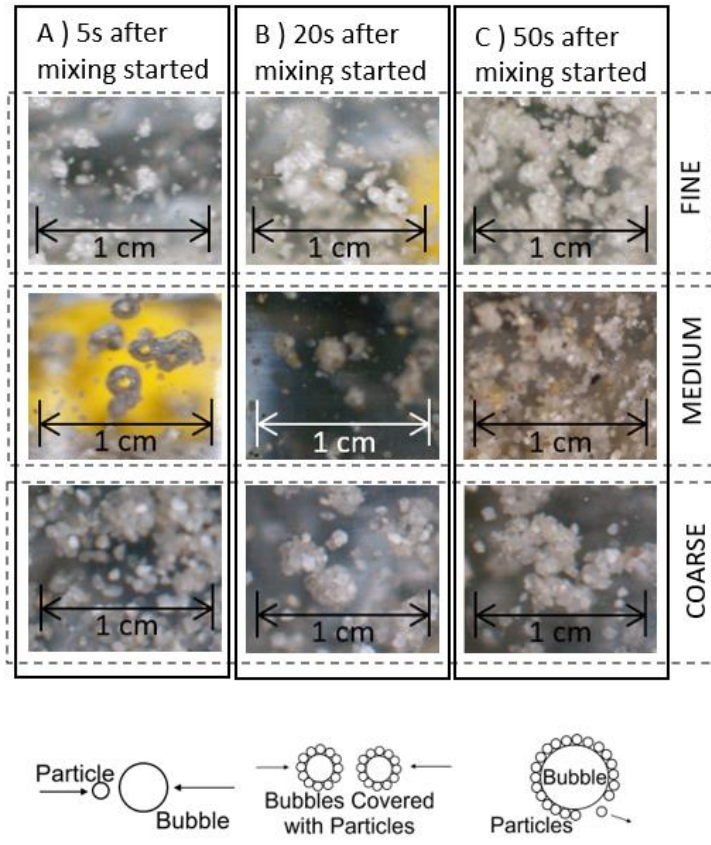
180 This section summarizes the liquid marble formation process and mechanisms, liquid marble's
181 physical appearance and size estimation after mixing, air entrapment, and final mixture density
182 reduction due to mixing.

183

184 **3.1 Liquid marble size and stability in post-wildfire mudflows**

185 On a millimeter scale, hydrophobic sand particles have a strong affinity to bond with air,
186 forming a heterogenous mixture with liquid marbles or particle-stabilized air bubbles and
187 preventing degasification (Aussillous and Quéré, 2001; Du et al., 2003; Bormaschenko, 2011;
188 McHale and Newton, 2011, 2015; Ong et al., 2021). Particle attachment, detachment, and
189 collision occur during liquid marble formation (**Figs. 2a-c**). For example, liquid marbles collide;
190 some merge into larger marbles, and others vanish. For example, **Fig. 2a** shows that only a few
191 particles are attached to bubbles within the first 5 s of mixing, and the rest are still floating in the
192 carrying fluid. At 20 s, more sand particles stick to air bubbles (**Fig. 2b**). Finally, particle-
193 covered bubbles collide and form super-large marbles. The initially wide marble size distribution
194 reduces and becomes more uniform after 50-s mixing (**Fig. 2c**).

195



196

197

198

199

200

201

202

203

204

205

206

207

208

Figure 2. Different sub-processes of particle-bubble interaction include particle bubble approaching, attachment, interactions, and detachment **a)** within the first 5 s, showing a diagram of particle-bubble attachment mechanisms; **b)** within 20 s, showing a diagram of marble-marble collision mechanism; and **c)** within 50 s after mixing started, showing marble-marble collision and particle-bubble separation mechanism.

This paper theoretically and experimentally investigates the formation process and stability of submerged liquid marbles composed of fine, medium, and coarse hydrophobic sands to understand conditions leading to mudflow air entrapment via liquid marbles. Modified Bond Number (Bo^*) can predict whether liquid marbles will form or not as stable under a specific set of conditions (see Supporting Information, Section S2). Table 2 summarizes the parameters used for calculating Bo^* . Assuming that the blade edge region has the most turbulent fluid flow

209 condition, the rotation length of a single particle's travel path is taken as the circle circumference
 210 that the blade sweeps by. The eddy turbulent accelerations (see Supporting Information, Eqn.
 211 S13) have different values since the equivalent downhill mixing velocities are different. **Fig. 3**
 212 plots the experimental Bo^* (see Supporting Information, Eqn. S12) for mean particle diameters
 213 of each sand with observed average bubble diameters inside liquid marbles that occurred at
 214 different mixing speeds against the theoretical Bo^* line at the value of one as a liquid marble
 215 stability criterion. Coarser sand particles and higher equivalent downhill mixing speed lead to
 216 $Bo^* > 1$, where liquid marbles become unstable, and particles detach from bubbles more easily.

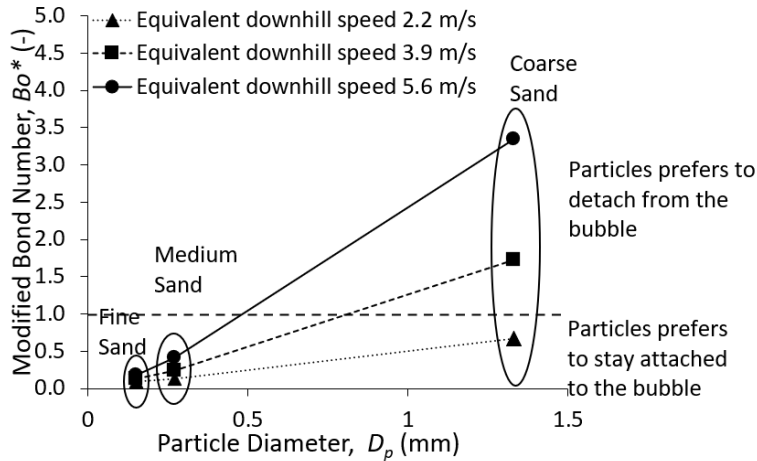
217

218 **Table 2.** Parameters for calculating the modified Bond number of liquid marbles

	Fine Sand			Medium Sand			Coarse Sand		
Particle Diameter (mm)	0.15			0.27			1.33		
Particle Density (kg/m^3)	2600			2600			2600		
Equivalent downhill mixing velocity (m/s)	3.11	5.44	7.78	3.11	5.44	7.78	3.11	5.44	7.78
Rotating Length Scale (m)	0.157								
Eddy Turbulent Acceleration (m/s^2)	62	188	385	62	188	385	62	188	385
Fluid Surface Tension (N/m)	0.07								
Average Contact Angle ($^\circ$)	91			91			91		
Bo^*	0.09	0.13	0.18	0.13	0.23	0.40	0.67	1.72	3.34

219

220



221

222 **Figure 3.** The combined effect of particle diameter D_p and equivalent downhill mixing speed on
 223 the modified Bo^* .

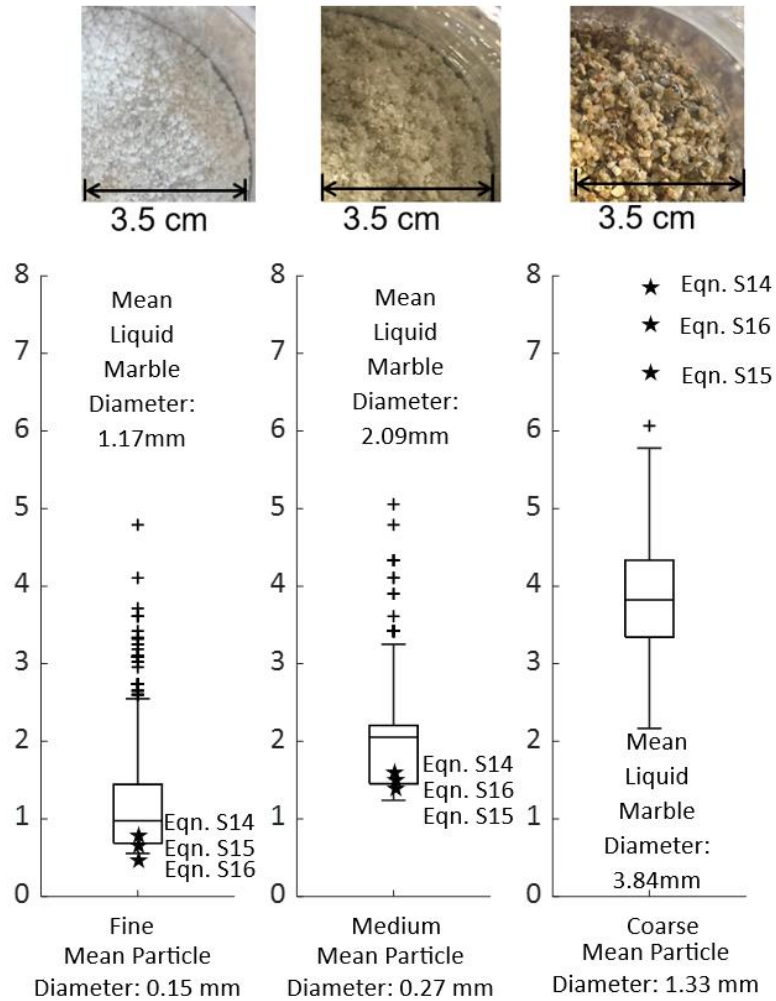
224

225 Although the modified Bo^* serves as estimate of likelihood in forming liquid marbles
 226 during various flow and transport conditions for different sands, the bubble stability estimation
 227 based on modified Bo^* has several limitations. First, the modified Bo^* only considers a particle
 228 at the bottom of the bubble. Second, Bo^* does not provide information about the liquid marble's
 229 size or shape. Third, air pressure and hydrodynamic pressure on the bubble are neglected, while
 230 Eqn. S2 (in Supporting Information) provides a more accurate calculation for balancing air
 231 pressure and hydrodynamic pressure. Fourth, the particle buoyancy exists at the partially
 232 submerged condition, so the approximation using a fully submerged condition is limited, and
 233 Eqn. S3 (in Supporting Information) addresses the issue. Fifth, the particle diameter is relatively
 234 restricted to a small range: between 0.15 mm and 0.25 mm for fine sand, between 0.25 mm and
 235 0.425 mm for medium sand, and between 1.18 mm and 1.70 mm for coarse sand. The soil in
 236 field conditions has a continuous particle diameter distribution of less than 0.075 mm up to 5 mm
 237 or above. Lastly, hydrodynamic drag is omitted. Therefore, a comprehensive analysis should

238 provide a better estimate of liquid marble stability using modified forces and considering
239 multiple particle-bubble locations and a complete set of forces.

240 Next, the applicability of theoretical Eqns. S14 - S16 (see Supporting Information,
241 section S3) to mudflow conditions liquid marbles is investigated in **Fig. 4**. For fine sand,
242 theoretically-predicted liquid marble diameters are 0.87 mm, 0.75 mm, and 0.45 mm,
243 respectively, based on Eqns. S14-S16 (see Supporting Information). Similarly, for medium sand
244 particles, the liquid marble diameters are 1.57 mm, 1.36 mm, and 1.49 mm, respectively. Finally,
245 the liquid marble diameters for coarse sand particles are 7.72 mm, 6.69 mm, and 7.30 mm,
246 respectively. **Fig. 4** shows positive analysis results for only a high shear rate of 778 s^{-1} where the
247 sand particle size strongly correlates with the final size of liquid marbles, where coarser
248 hydrophobic sand leads to larger marbles. **Fig. 4** results are selected among various tested mixing
249 times, equivalent downhill mixing speeds, and initial solid volumetric concentrations.

250



251

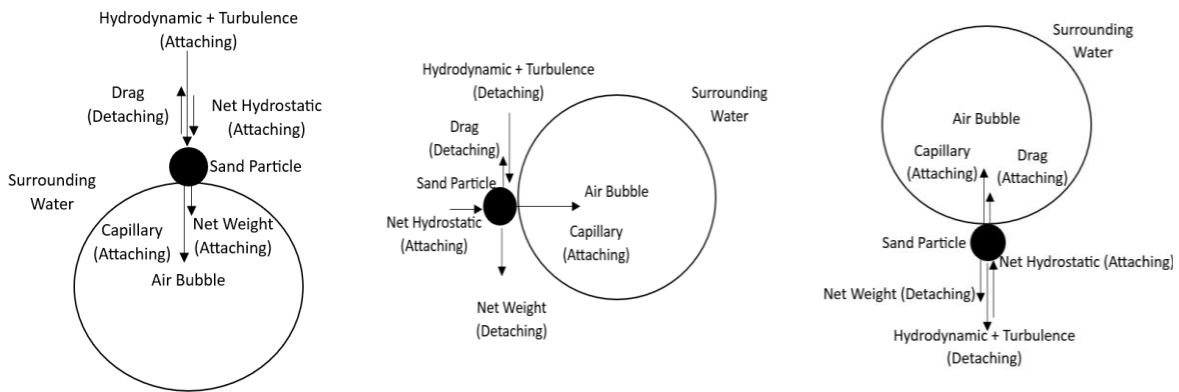
252 **Figure 4.** Effect of the sand particle size on the liquid marble size. The results include all initial
 253 solid concentrations at the high end of 778 s^{-1} , which produces the most stable liquid marbles.
 254 The mixing time is cut after the equilibrium condition: $> 60 \text{ s}$ for fine sand and $> 40 \text{ s}$ for
 255 medium and coarse sand.

256

257 Since Bo^* and Eqns. S14 – S16 are limited in the prediction of sizes and stabilities of
 258 liquid marbles in mudflows, a comprehensive force analysis is proposed to identify a full set of
 259 conditions in liquid marble formations for post-wildfire mudflow-like mixtures. The analysis
 260 quantifies the forces that affect liquid marble formation and uses static and dynamic equilibrium

261 to understand better liquid marble stability constrained to post-wildfire mudflow conditions.
 262 Since a single hydrophobic sand particle can attach to a bubble anywhere on the surface,
 263 different scenarios that can be used to study force balance are investigated. In **Fig. 5a**, a
 264 hydrophobic sand particle stays at the top of the bubble; in **Fig. 5b**, a particle stays at the
 265 left/right side of the bubble, which is the worst-case scenario considering the hydrodynamic
 266 effects in horizontal fluid flow; and in **Fig. 5c** a particle stays at the bottom of the bubble which
 267 is not favorable when gravity dominates over inertial forces.

268



269

270 **Figure 5.** Examples of Forces under different scenarios with different particle-bubble relative
 271 locations: **a)** sand particle on the top of the bubble, **b)** sand particle to the left of the bubble, and
 272 **c)** sand particle at the bottom of the bubble.

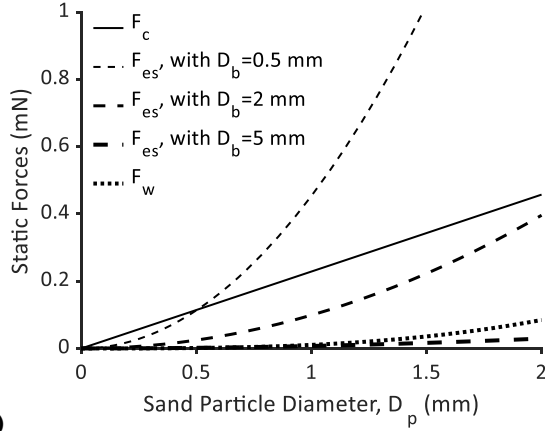
273

274 Many forces are involved in particle-bubble interaction (see Supporting Information,
 275 Eqns. S1-S11). Three types of static forces dominate in the particle-bubble interaction process
 276 (**Fig. 6a**): capillary force, excess force, and net weight force. Capillary force favors particle-
 277 bubble attraction (Tao, 2005) and linearly depends on the sand particle diameter (**Fig. 6a**). The
 278 excess force acts as an attractive force when the bubble diameter is smaller than 5.5 mm (Tao,

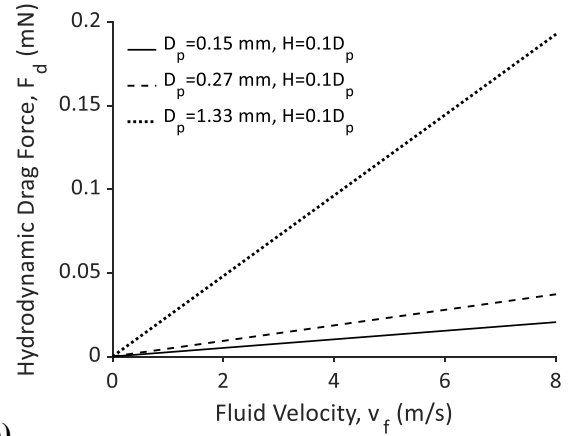
279 2005) and is a function of the sand particle diameter squared as shown by Eqn. S2 (see
280 Supporting Information). Smaller bubbles experience stronger attractive net hydrostatic forces.
281 The net weight is generally a repulsive force (Tao, 2005). The net weight force (**Fig. 6a**) has a
282 cubic relationship with the sand particle diameter since both the weight and buoyancy parts of
283 the equation depend on the sand particle volume. For all three forces, Young's contact angle
284 applies. Two major hydrodynamic forces exist in the particle-bubble interaction process:
285 hydrodynamic drag force (**Fig. 6b**) and local turbulence force (**Figs. 6e-g**). In drag calculation
286 here, an estimate of drag reduction of 25% is applied. Hydrodynamic drag force is a repulsive
287 force (Tao, 2005). Drag force is linearly dependent on fluid velocity (**Fig. 6b**). The undisturbed
288 fluid flow velocity is assumed to be the same as the velocity provided by the impeller. The
289 particle slip velocity is obtained from Stokes' rule. The drag force is larger on coarser particles.

290 Reynolds number of the fluid flow during the mixing process is a function of impeller
291 diameter, liquid density, liquid dynamic viscosity, and velocity provided by the impeller (Paul et
292 al., 2004). The mixing process becomes turbulent when the Reynolds number exceeds 10,000
293 (Paul et al., 2004), which occurs at impeller velocities higher than 4 m/s in this experiment.
294 Therefore, the local turbulence force is only considered in a turbulent flow regime. Flow
295 direction allows hydrodynamic force on particles to attach or detach from the bubble (**Figs. 6c-**
296 **d**). Instead of plotting hydrodynamic force only, this figure plots the ratio between
297 hydrodynamic force and the sum of all other static forces. The calculation takes the air bubble as
298 a fixed reference point. Therefore, the u_{pb} is the relative velocity between the sand particle and
299 the bubble. The particle velocity is induced by surrounding fluid obtained from Eqns. S4-S9 (see
300 Supporting Information). In case 1 defined in **Fig. 5a**, the sand particle is above the air bubble
301 (hydrodynamic force analysis in **Fig. 6c**). Therefore, net weight, capillary, and excess forces
302 attach forces in which the overall acting direction is downward. When hydrodynamic impact

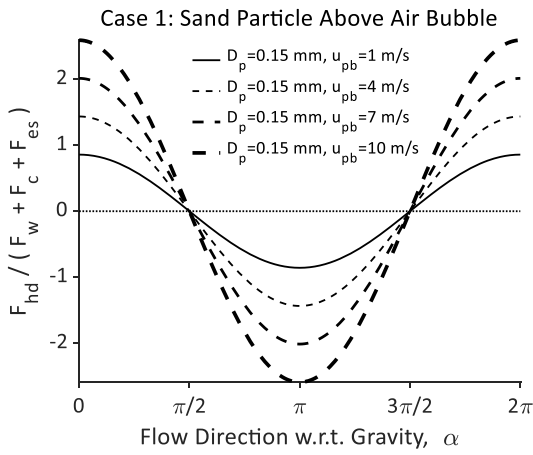
303 angle α equals 0 or 2π , the flow direction is parallel to gravity or the overall acting direction of
304 all static forces. When α equals π , the flow direction is perpendicular to gravity. When the
305 hydrodynamic drag force has the same direction as the overall acting direction of all static forces
306 ($0 < \alpha < \pi/2$, or $3\pi/2 < \alpha < 2\pi$), a more attaching particle-bubble interaction will occur. When
307 hydrodynamic drag force is in the opposite direction of the overall acting direction of all static
308 forces ($\pi/2 < \alpha < 3\pi/2$), a detaching particle-bubble interaction will occur. In case 2 defined in
309 **Fig. 5c**, the sand particle is below the air bubble (hydrodynamic force analysis in **Fig. 6d**).
310 Therefore, net weight has a detaching effect, while capillary and excess forces have an attaching
311 effect. The overall acting direction of all static forces is still towards the bubble center (upward,
312 favoring attractive interaction). The hydrodynamic effect is opposite to case 1. While the
313 hydrodynamic impact angle is between $3\pi/2$ and 2π , the hydrodynamic drag force has an
314 attaching effect in particle-bubble interaction. Otherwise, the hydrodynamic drag force causes
315 the detaching effect. The analysis considers local turbulence force an additional enhancement of
316 hydrodynamic drag force. In the force equilibrium analysis, the local turbulence force only
317 applies when the impeller-induced Reynolds number exceeds 10,000. **Figs. 6e-g** show how local
318 turbulent force depends on bubble diameter, sand particle diameter, and fluid energy dissipation.
319 As bubble size increases, the local turbulence force decreases. However, local turbulence force
320 increases as sand particle diameter or fluid energy dissipation increases.
321



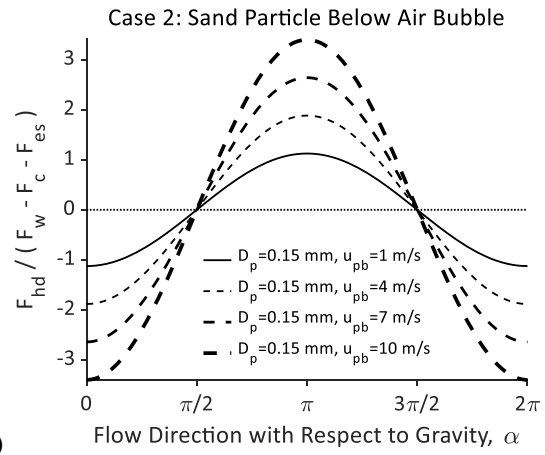
a)



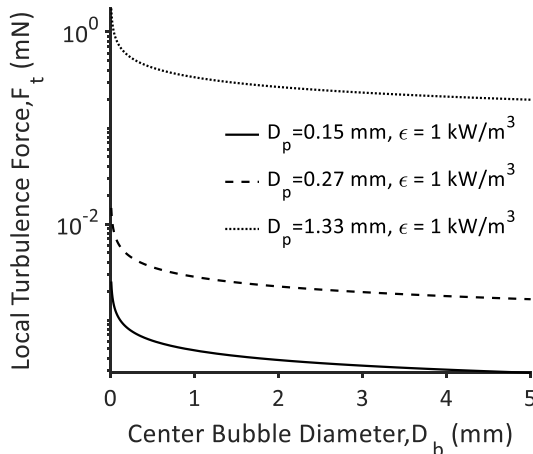
b)



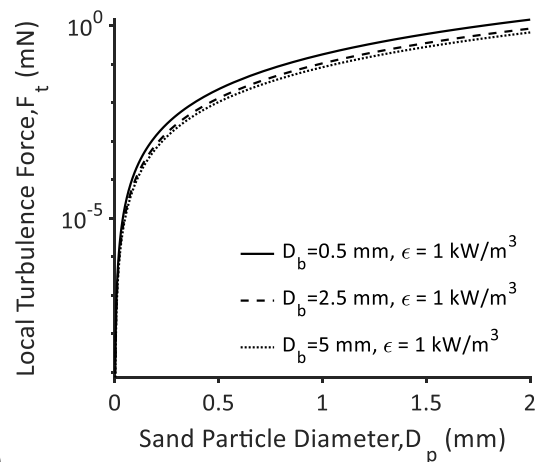
c)



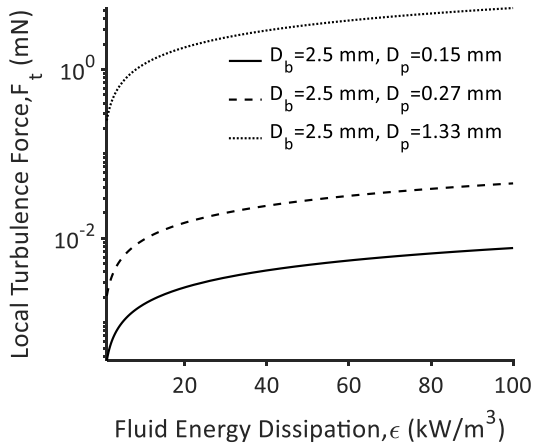
d)



e)



f)

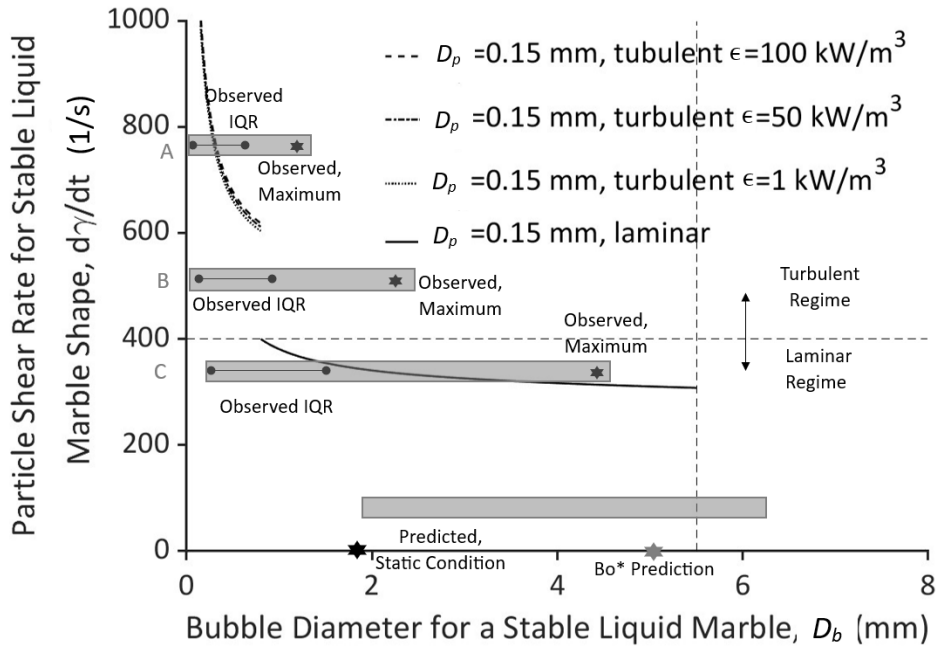


322 **Figure 6.** Static and Dynamic forces in particle bubble interaction process. **a)** capillary, excess
 323 static, and weight forces, where D_b is the bubble diameter. **b)** hydrodynamic drag forces. **c)**
 324 effect of hydrodynamic impact angle when the particle is above the bubble, **d)** effect of
 325 hydrodynamic impact angle when the particle is below the bubble, **e)** local turbulence force due
 326 to the effect of bubble diameter, **f)** local turbulence force due to the effect of sand particle
 327 diameter, **g)** local turbulence force due to the effect of fluid energy dissipation.

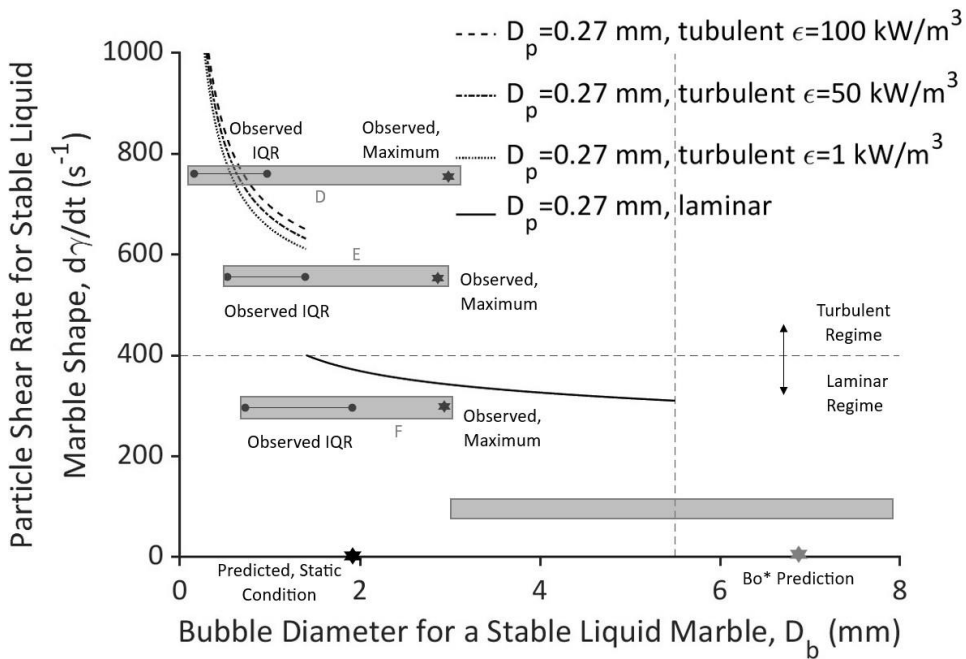
328

329 **Figs. 7a-c** quantify results of force balance analysis between capillary, net hydrostatic,
 330 hydrodynamic, and local turbulence forces. The shear rate and bubble diameter relationship at a
 331 condition of a stable liquid marble, specifically for a single-bubble-single-particle interaction
 332 process, is obtained from the force equilibrium. The system is turbulent for all three sand sizes
 333 when the particle shear rate exceeds 400 s^{-1} and laminar when the particle shear rate is less than
 334 400 s^{-1} . The cutoff bubble diameter for the analysis is 5.5 mm.

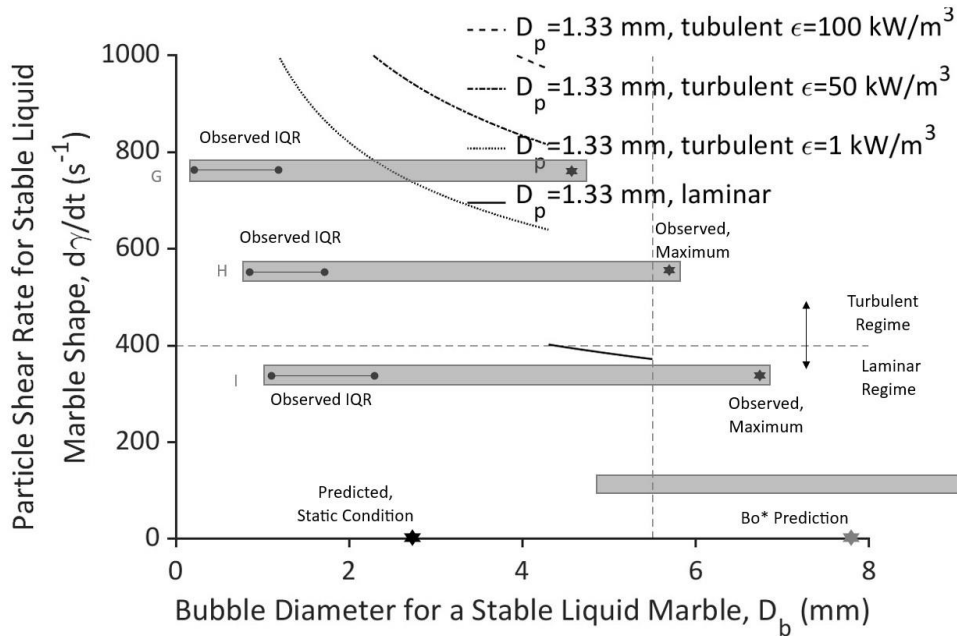
335



a)



b)



c)

336

337 **Figure 7.** Particle shear rate vs. bubble diameter for a stable liquid marble (single-particle-
 338 single-bubble interaction) based on force equilibrium analysis: **a)** fine sand particles, **b)** medium
 339 sand particles, **c)** coarse sand particles.

340

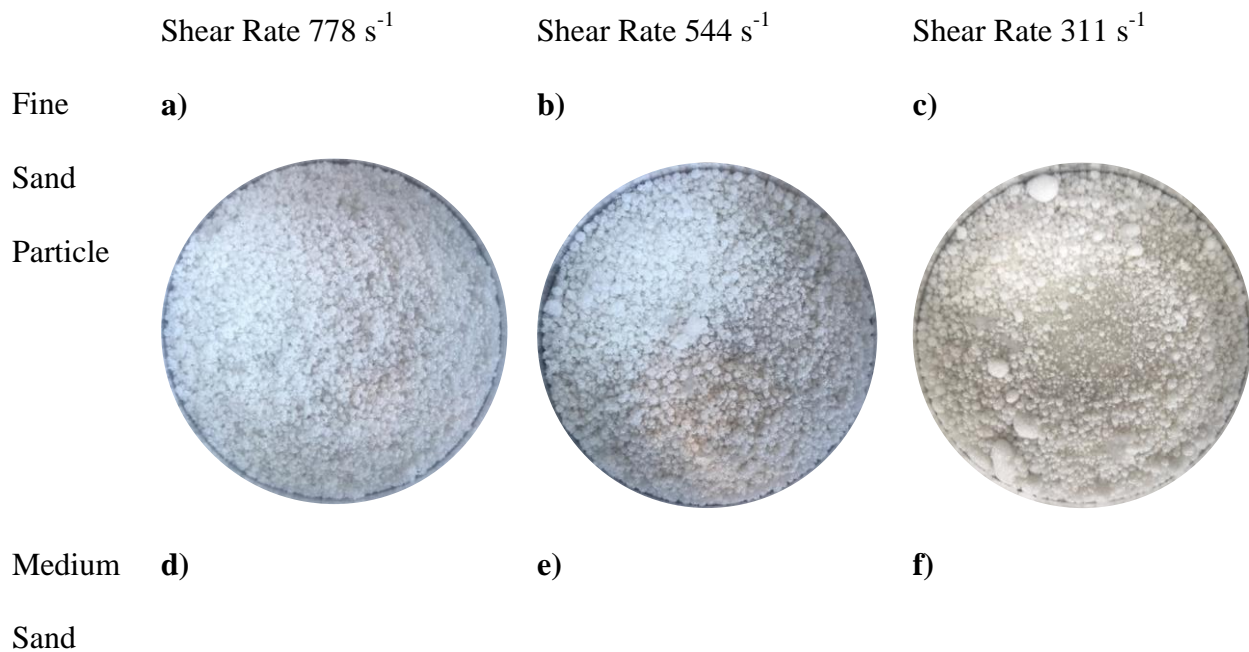
341 Liquid marbles covered with fine sand particles (**Fig. 7a**) have the largest stable diameter
 342 range between 1 and 5.5 mm in a laminar environment among all three types of sand. The
 343 analysis (see star dots on the x-axis in Figs. 9a-c) predicts a stable liquid marble diameter of
 344 about 1.8 mm using the same forces equations but without the hydrodynamic effect. With a fixed
 345 mixing time and a fixed initial solid volumetric concentration ratio, the interquartile range (IQR,
 346 or middle 50% and is defined as the difference between the 75% and 25% of the data) of
 347 observed liquid marble completely falls below the equilibrium-analysis predicted line for the
 348 lowest shear rate of 311 s^{-1} (Cup A, also in **Fig. 8a**). However, the maximum observed liquid
 349 marble diameter falls to the right side of the prediction curve. For higher shear rates of 544 s^{-1}

350 (Cup B, also in **Fig. 8b**) and 778 s^{-1} (Cup C, also in **Fig. 8c**), the IQR of observed liquid marbles
351 will cross the prediction curve further away. Note that the maximum observed liquid marble
352 diameters both fall to the right side of the curve. For liquid marbles covered with medium sand
353 particles (**Fig. 7b**), the range of stable bubble diameter in a laminar environment is narrower,
354 from 1.5 to 5.5 mm. The stable bubble diameter range is smaller for medium sand compared with
355 fine sand conditions. Without a hydrodynamic effect, the stable liquid marble has a predicted
356 bubble diameter of about 1.9 mm. The liquid marble diameter under three different shear rates
357 for medium sand particles is similar to the cases for fine sand particles. The only difference is
358 that the maximum observed liquid marble diameter under the shear rate of 311 s^{-1} (Cup D, also in
359 **Fig. 8d**) is still within the curve boundary. However, it is very close to the boundary. Observed
360 liquid marble diameters exceed the prediction limit for shear rates at 544 s^{-1} (Cup E, also in **Fig.**
361 **8e**) and 778 s^{-1} (Cup F, also in **Fig. 8f**). For liquid marble covered with coarse sand particles
362 (**Fig. 7c**), the range of stable bubble diameter in a laminar environment is the shortest, from 4 to
363 5.5 mm. The stable bubble diameter range is the smallest for coarse sand. That means the liquid
364 marble stability is the worst for coarse sand among all three types of sand particles. Without
365 hydrodynamic effects, the stable liquid marble has a predicted bubble diameter of about 2.6 mm.
366 The IQR of the observed liquid marble still falls within the prediction limit. However, unlike the
367 other two types of sand particles, the maximum observed liquid marbles all fall to the right side
368 of the prediction curve (Cup G, also in **Fig. 8g**; Cup H, also in **Fig. 8h**; Cup I, also in **Fig. 8i**).
369 Overall force equilibrium analysis and experimental data match well, where experimental data
370 show a range of liquid marble diameters. Roughly 70% of the Interquartile Range (IQR) of
371 observed liquid marbles falls within the prediction, meaning most of the liquid marbles obtained
372 from the experiment still follow the general principle of force balances for single-particle-single-
373 bubble interaction. Multiple-particle-single-bubble interaction (Wang et al., 2022) and liquid-

374 marble-liquid-marble interaction (Jin et al., 2018), particle diameter discrepancies due to sieve
375 sizes, roundness, and sphericity variances are the possible reasons for the observed ranges.

376 For fine sand particles with an average diameter of 0.15 mm, the average estimated
377 bubble diameter of the final liquid marble covered by fine sand is about 0.96 mm using the force
378 balance method and the three direct estimation equations (see Supporting Information, Eqns.
379 S14-S16) mentioned previously in this paper. Therefore, the collision efficiency (see Supporting
380 Information, Eqn. S17) for a single fine sand particle to collide with a bubble is 0.47. Medium
381 sand particles have an average diameter of 0.27 mm. The average estimated bubble diameter of
382 the final liquid marble covered by medium sand is about 1.33 mm. Thus, the collision efficiency
383 for a single medium sand particle to collide with a bubble is 0.61. Coarse sand particles have an
384 average diameter of 1.33 mm. The average estimated bubble diameter of the final liquid marble
385 covered by coarse sand is about 6.12 mm. The collision efficiency for a single coarse sand
386 particle to collide with a bubble is 0.65.

387



Particle



Coarse

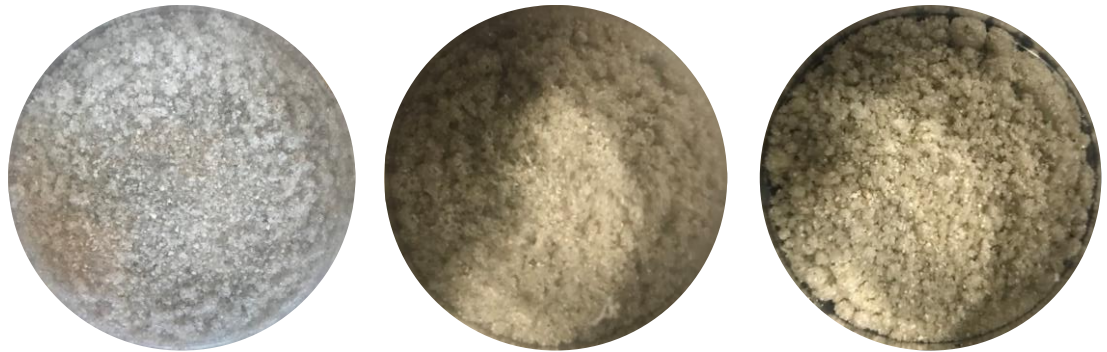
g)

h)

i)

Sand

Particle



388

389 **Figure 8.** Top Views of Cups A to I in Figure 8.

390

391 **3.2 Evaluation of the mixture air entrapment and density**

392 The total volume of air trapped in hydrophobic liquid marbles within mixtures is quantified with
393 the specific air content (Eqn. 4), and thus, the bulk density of hydrophobic sand slurries
394 decreases compared to hydrophilic sand slurries. The entrapped air in the three-phase mixture is
395 measured by subtracting the initial water and solid volumes from the total final mixture. The
396 measurement error of volume falls within +/- 1 mL. Table 3 shows a comparison of air
397 entrapments produced with hydrophobic and hydrophilic fine, medium, and coarse sands for a
398 mixing time of 10 – 120 seconds, a shear rate of 311 – 778 s⁻¹, and an initial solid volumetric
399 concentration of 5 – 25%. As introduced at the beginning of the article, debris flows with regular

400 hydrophilic soil can entrap air bubbles if the debris flow impacts an obstacle (Lugni et al., 2006;
 401 Song et al., 2021) or wave surges (Arguden & Rodolfo, 1990); however, it can be seen that
 402 hydrophilic sand does not have as strong capability to trap air during the mixing process as
 403 hydrophobic sand.

404

405 **Table 3.** A comparison of air entrapment with hydrophobic and hydrophilic sand under selected
 406 conditions. V_s is the volume of sand particles, V_w is the volume of water, and e^* is the specific air
 407 content.

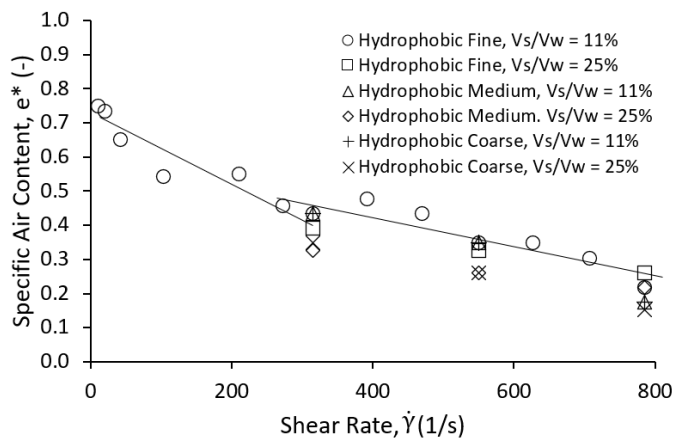
Sand Particle Type	V_s/V_w	Shear Rates	Mixing Time	e^* for Hydrophilic sand	e^* for Hydrophobic Sand
	(%)	(s^{-1})	(s)	(%)	(%)
Fine	5	778	60	0.0	17
Fine	11	778	60	4.3	22
Fine	18	778	60	2.9	23
Fine	25	778	60	4.3	27
Fine	25	778	10	6.5	70
Fine	25	778	120	4.3	15
Fine	25	544	60	4.3	39
Fine	25	311	60	6.5	49
Medium	5	778	60	0.0	13
Medium	11	778	60	0.0	19
Medium	18	778	60	2.9	20
Medium	25	778	60	4.3	22
Medium	25	778	10	4.3	43
Medium	25	778	80	2.2	18
Medium	25	544	60	4.3	26
Medium	25	311	60	4.3	33
Coarse	5	778	60	0.0	9
Coarse	11	778	60	0.0	12
Coarse	18	778	60	2.9	13
Coarse	25	778	60	2.2	16
Coarse	25	778	10	4.3	48
Coarse	25	544	60	2.2	26
Coarse	25	311	60	4.3	35

408

409

410 **Fig. 9** shows the correlation between the specific air content and shear rate. When the
 411 shear rate increases, the specific air content decreases. The decreasing behavior of air entrapment
 412 changes at around 300 s^{-1} . Before this separating shear rate, air entrapment decreases faster as the
 413 shear rate increases. Low mixing power at a low shear rate causes more uneven mixing results,
 414 leading to extremely diverse physical appearances of liquid marbles, as shown in **Figs. S4a-b**
 415 (see Supporting Information). When mixing at high shear rates, the mixing powers are strong
 416 enough to cause a more uniform physical appearance of marbles (**Figs. S4c-f**, see Supporting
 417 Information). Hydrodynamic forces from mixing speed must be coupled with other forces, such
 418 as resisting forces due to gravity, at low shear rates when investigating their effect on air
 419 entrapment. Group "Hydrophobic Fine, $V_s/V_w = 11\%$ " provides the range of shear rates to form
 420 stable liquid marbles.

421



422

423 **Figure 9.** Specific air content vs. shear rate, where all the experiments mixing exceeds 60
 424 seconds.

425

426 **Fig. 10** further quantifies how the mixing time decreases trapped air aiming towards the
 427 equilibrium state by partial degassing. The equilibrium state is defined as the internal structure of

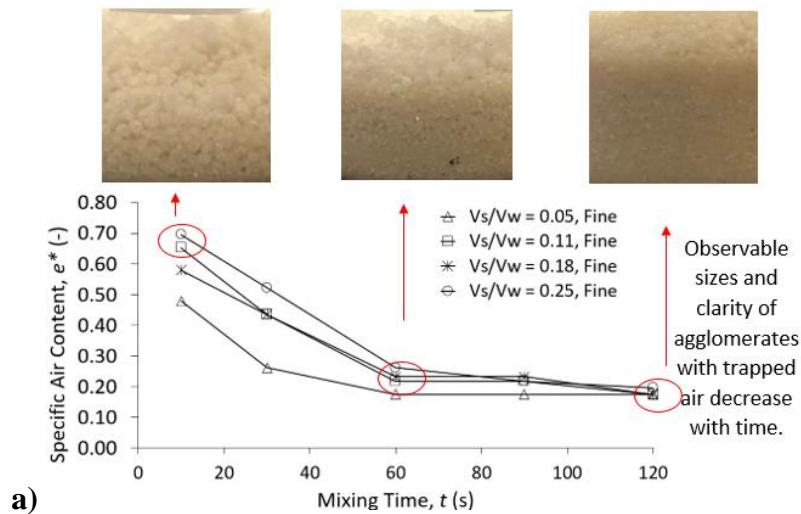
428 the mixture that is stable against longer and more vigorous mixing, characterized by stable liquid
 429 marbles shown in **Fig. S4g** (see Supporting Information). **Figs. 10a-c** show that with smaller
 430 diameters and less observable in some cases, liquid marbles form when the mixture undergoes
 431 prolonged mixing. It can be seen that coarser sand needs less time to reach the equilibrium, and
 432 higher initial solid concentration mixes need a longer time to reach the equilibrium state. **Fig.**
 433 **10d** synthesizes coupled effects and serves as a base for the proposed empirical relationship:

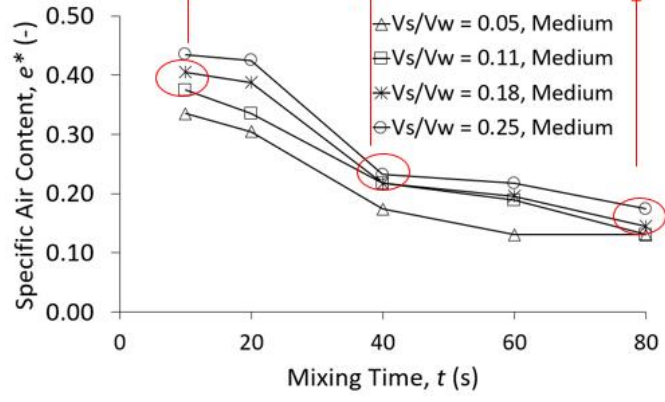
$$\frac{e^*}{V_s/V_w} = 4.44(tD_p)^{-0.31} \quad (5)$$

434 **Fig. 10e** describes an empirical correlation between air entrapment normalized by initial solid
 435 volumetric concentration and Bo^* , which depends on the mean particle diameter and mean
 436 velocity (see Supporting Information, Eqn. S12). Therefore, besides describing the time effect on
 437 the specific air content, this paper proposes another empirical correlation focusing on the
 438 velocity effect on the specific air content:

$$\frac{e^*}{V_s/V_w} = -0.56 \ln Bo^* + 1.92 \quad (6)$$

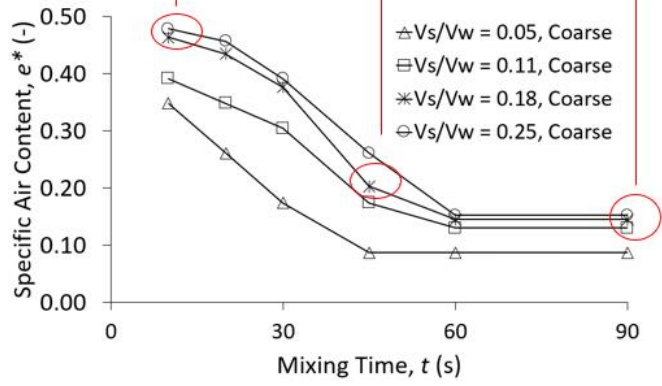
439





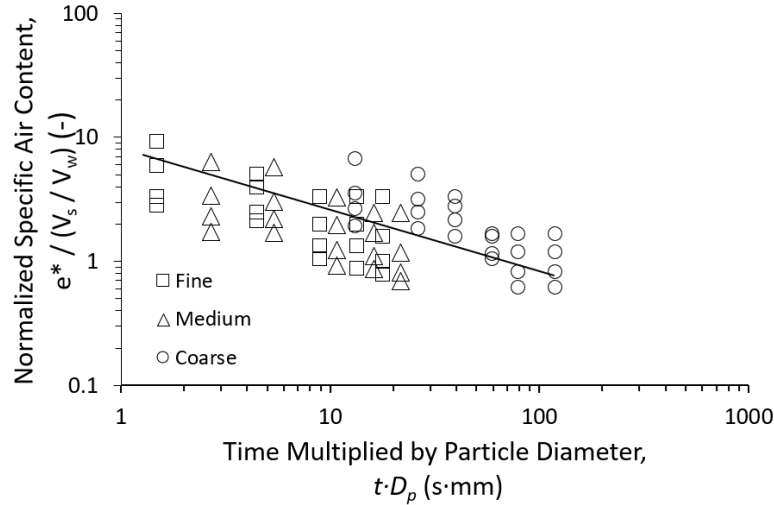
441

b)



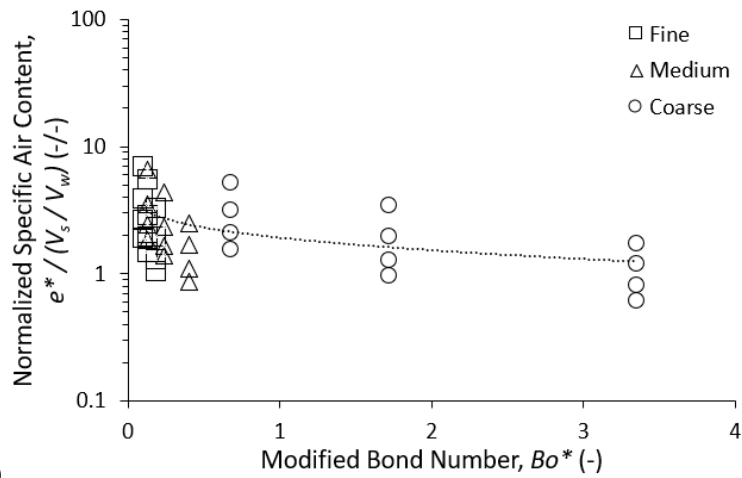
442

c)



443

d)



444

e)

445 **Figure 10.** Coupled effect mixing time and types of sand particles on the ability to trap air phase
 446 for **a)** fine sand particles, **b)** medium sand particles, **c)** coarse sand particles, and **d)** combined
 447 results. **e)** Empirical correlation between specific air content normalized by initial solid
 448 volumetric concentration and modified Bond Number.

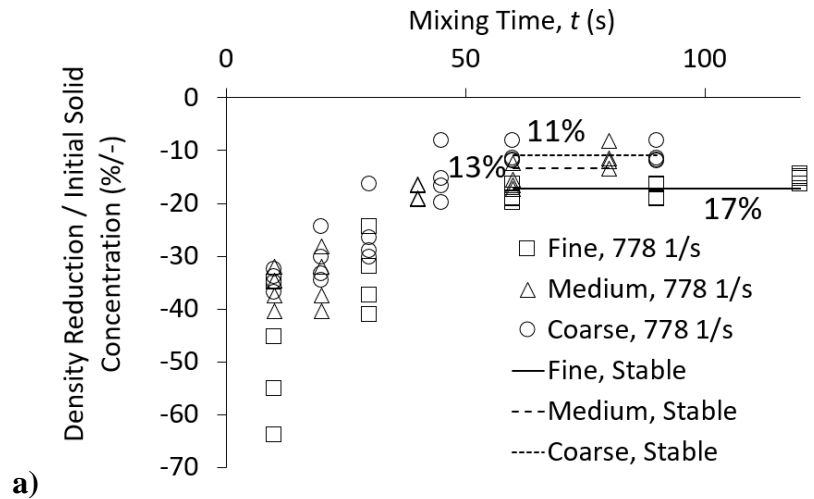
449

450 Besides air entrapment as an essential indicator of the mixing behavior of hydrophobic
 451 particles, water, and air, density change before and after mixing is necessary for mudflow
 452 models. The density reduction indicates how much water-sand slurry will reduce due to the
 453 additional entrapment of air phases when the same amount of sand becomes hydrophobic. **Fig.**

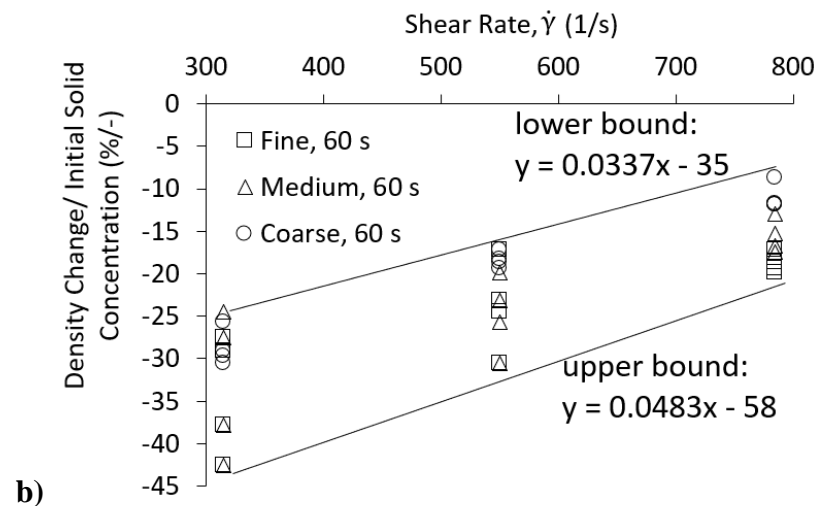
454 **11a** shows the effect of mixing time on the density changes of the final mixture. The density
 455 reduction will reach a stable condition for the extended mixing time, which is shorter for coarser
 456 particles. The average final density reduction is 17%, 13%, and 11% for fine, medium, and
 457 coarse sand particles, respectively, when the shear rate is 778 s^{-1} (i.e., the equivalent downhill
 458 mixing speed is 7.8 m/s). After ruling out the time effect, shear rate consistently impacts all types
 459 of sand (**Fig. 11b**). **Fig. 11b** defines two bounding equations as a speed function to provide a
 460 range of estimation of density change normalized by initial solid concentration.

461

462



463



464 **Figure 11.** Density reduction due to **a)** mixing time and **b)** shear rate.

465

466 **4 Discussion and Conclusions**

467 This paper investigated complex mixtures that contain water, hydrophobic sand, and entrapped
468 air. For the first time, this research identified conditions that control air trapping into postwildfire
469 mudflows due to mechanisms enhanced by the wildfire-induced soil hydrophobicity. During
470 wildfires, a surficial layer of non-cohesive sandy soils turns hydrophobic due to the deposition of
471 organic combustion matter on the particle surface. Upon subsequent rain, erosion and mudflows
472 form easily, causing devastating hazards. The air-trapping occurs due to the hydrophobic sand
473 particles attaching to the air bubbles attracted into the mixture, forming liquid marbles in water.
474 This paper shows that sand particles and water are not necessarily only mudflow constituents in
475 hydrophobic slopes because hydrophobic sands have a high capacity to entrap air via liquid
476 marbling mechanisms—an extensive controlled laboratory program aided in understanding
477 liquid marble formation and stability evolution in dense mixtures. The relationship between
478 density change and parameters that can be back-estimated from field analysis, such as average
479 flow velocity in a sloped hill or average solid concentration, have been developed. Fine, medium,
480 and coarse hydrophobic sands represent three different grains of sand as categorized from a
481 geotechnical perspective.

482 This paper quantified and compared the effects of coupled equivalent downhill mixing
483 speeds, mixing time, sand particle type, and variations in initial air-water-solid volumetric ratios
484 on air entrapment. In addition, the experiments confirm findings from Cervantes-Álvarez et al.
485 (2020), which showed that an initial solid volumetric concentration dominates the final air
486 trapping volume over any other tested factors. Specifically, the initial solid volumetric
487 concentration dominates over shear rates (311 to 778 s⁻¹), shear time (10 to 120 s), and sand
488 particle types (fine, medium, or coarse) in the current study. For the first time, the paper proposes

489 a forecasting formula for mudflow density for a sand-dominated site under various mixing
490 conditions. Specific new findings show that a longer mixing time gradually decreases the amount
491 of entrapped air. Mixing time affects amount of air and relates to the time from the start rain-
492 induced erosion on burned scar with hydrophobic particles to later times of mudflow dynamics.
493 In addition, mixing time is coupled with the average particle size, and coarser sand needs
494 consistently less mixing time than fine sands to reach a steady volume of trapped air in the
495 mixture at all investigated equivalent downhill mixing speeds. Collision efficiency between a
496 particle and a bubble is higher for coarser sands. Next, considering the mixing rate, air trapped in
497 the mixture decreases as the mixing velocity and sand coarseness increase. Observing air bubbles
498 and liquid marbles can explain the variation and decrease of entrapped air in the mixture under
499 faster, longer mixing and with coarser hydrophobic sands. Coarser sand forms larger liquid
500 marbles than finer sand, with larger modified Bond number, which indicates higher initial bubble
501 shape irregularities where larger marbles deform more and break more easily. Liquid marble
502 breakage is more prominent at a higher speed with a longer mixing time in coarser sand than in
503 other sand. This experiment provides evidence that local turbulence and flow instabilities make
504 particle-bubble interaction more unpredictable and increase the vulnerability of formed liquid
505 marbles toward breakage. As mixing velocity increases, experimental observation deviates more
506 from theoretical calculation. Besides, as mixing velocity increases, larger liquid marbles are hard
507 to survive.

508 The experiments shown in this paper specialize in narrow particle size to investigate the
509 role of particle size in air entrapment. Although the small-scale mixing experiments in this
510 research are limited compared to site and large-scale soil heterogeneity, they provide an excellent
511 baseline. Experiments show that coarser sand reduces the volume of entrapped air, and with
512 gravel or boulders, air entrapment could be less, because gravity forces from gravels or boulders

513 and hydrodynamic forces from large particles can easier break the multiphase force balance
514 among air bubbles, water, and solid particles. With less entrapped air and smaller density
515 reduction, the upper bound equation does not change, and the lower bound equation will shift
516 upwards. Since the experiments only consider sand particles, the amount of trapped air could be
517 different if the mixture contains hydrophilic particles and sand, or clays.

518

519 **Acknowledgments**

520 Financial support provided by the U.S. National Science Foundation, Division of Chemical,
521 Bioengineering, Environmental, and Transport Systems under NSF CBET Grant No. 2025643 is
522 gratefully acknowledged. The authors do not have any conflict of interest. We acknowledge
523 Melisa Lepe for helping with experiments and Haohua Chen and Mahta Movasat for giving
524 constructive feedback on the paper. We thank Haohua Chen for proofreading.

525

526 **Open Research**

527 Data – Our recorded data, Excel files, and MATLAB code files can be downloaded
528 [<https://ingridtomac.eng.ucsd.edu/foldershare/6101>].

529 Software – Analysis and figures were done with Microsoft Excel and MATLAB version R2023a.

530 The MATLAB license is available at: <https://mathworks.com/>.

531

532 **References**

- 533 1. Abatzoglou, J. T. & Williams, A. P. (2016). Impact of anthropogenic climate change on
534 wildfire across western U.S. forests. *Proceedings of the National Academy of Sciences*,
535 *113*(42), 11770–11775. <https://doi.org/10.1073/pnas.1607171113>

- 536 2. Arguden, A.T., & Rodolfo, K. S. (1990). Sedimentologic and dynamic differences
537 between hot and cold laharic debris flows of Mayon Volcano, Philippines. *Geological*
538 *Society of America Bulletin*, 102(7), 865–876. [https://doi.org/10.1130/0016-](https://doi.org/10.1130/0016-7606(1990)102<0865:saddbh>2.3.co;2)
539 [7606\(1990\)102<0865:saddbh>2.3.co;2](https://doi.org/10.1130/0016-7606(1990)102<0865:saddbh>2.3.co;2)
- 540 3. Aussillous, P., & Quéré, D., (2001). Liquid marbles. *Nature*, 411(June), 924–927
- 541 4. Bisdom, E.B.A., Dekker, L.W., & Schoute, J.F.Th. (1993). Water repellency of sieve
542 fractions from sandy soils and relationships with organic material and soil structure.
543 *Geoderma*, 56(1-4), 105-118. [https://doi.org/10.1016/0016-7061\(93\)90103-R](https://doi.org/10.1016/0016-7061(93)90103-R).
- 544 5. Bormaschenko, E., (2011). Liquid marbles: Properties and applications. *Current Opinion*
545 *in Colloid & Interface Science*, 16(4), 266-271.
- 546 6. Bull, W. B. (1963). Alluvial-fan deposits in western Fresno County, California. *The*
547 *Journal of Geology*, 71(2), 243–251. <https://doi.org/10.1086/626896>
- 548 7. Cannon, S. H., Gartner, J. E., Wilson, R. C., Bowers, J. C., & Laber, J. L. (2008). Storm
549 rainfall conditions for floods and debris flows from recently burned areas in southwestern
550 Colorado and Southern California. *Geomorphology*, 96(3-4), 250–269.
551 <https://doi.org/10.1016/j.geomorph.2007.03.019>
- 552 8. Cannon, S. H., Kirkham, R. M., & Parise, M. (2001). Wildfire-related debris-flow
553 initiation processes, Storm King Mountain, Colorado. *Geomorphology*, 39(3-4), 171–188.
554 [https://doi.org/10.1016/s0169-555x\(00\)00108-2](https://doi.org/10.1016/s0169-555x(00)00108-2)
- 555 9. Cervantes-Álvarez, A. M., Escobar-Ortega, Y. Y., Sauret, A., & Pacheco-Vázquez, F.
556 (2020). Air entrainment and granular bubbles generated by a jet of grains entering water.
557 *Journal of Colloid and Interface Science*, 574, 285–292.
558 <https://doi.org/10.1016/j.jcis.2020.04.009>

- 559 10. Conedera, M., Peter, L., Marxer, P., Forster, F., Rickenmann, D., & Re, L. (2003).
560 Consequences of forest fires on the hydrogeological response of mountain catchments: A
561 case study of the Riale Buffaga, Ticino, Switzerland. *Earth Surface Processes and*
562 *Landforms*, 28(2), 117–129. <https://doi.org/10.1002/esp.425>
- 563 11. Cui, Y., Cheng, D., & Chan, D. (2018). Investigation of post-fire debris flows in
564 Montecito. *ISPRS International Journal of Geo-Information*, 8(1), 5.
565 <https://doi.org/10.3390/ijgi8010005>
- 566 12. DeBano, L.F., Osborne, J.F., Krammes, J.S., & Letey, L.(1967). Soil wettability and
567 wetting agents ... our current knowledge of the problem. USDA Forest Service Research
568 Paper PSW-43, Pacific Southwest Forest and Range Experiment Station, Berkeley, CA
- 569 13. DeBano, L.F., Savage, S.M., & Hamilton, D.A. (1976). The transfer of heat and
570 hydrophobic substances during burning. *Soil Science Society of America Journal*, 40,
571 779-782
- 572 14. DeBano, L. F., Rice, R. M., & Eugene, C. C. (1979). Soil heating in chaparral fires:
573 effects on soil properties, plant nutrients, erosion, and runoff. Res. Paper PSW-RP-145.
574 Berkeley, CA: U.S. Department of Agriculture, Forest Service, Pacific Southwest Forest
575 and Range Experiment Station.
- 576 15. DeBano, L. F. (1981). Water repellent soils: a state-of-the-art. Gen. Tech. Rep. PSW-
577 GTR-46. Berkeley, CA: U.S. Department of Agriculture, Forest Service, Pacific
578 Southwest Forest and Range Experiment Station.
- 579 16. DeBano, L. F. (1991). The effect of fire on soil properties. In: Harvey, Alan E.;
580 Neuenschwander, Leon F., compilers. Proceedings-management and productivity of
581 western-montane forest soils; 1990 April 10-12; Boise, ID. Gen. Tech. Rep. INT-280.

582 Ogden, UT: U.S. Department of Agriculture, Forest Service, Intermountain Research
583 Station.

584 17. DeBano, L. F. (2000a). The role of fire and soil heating on water repellency in Wildland
585 Environments: A Review. *Journal of Hydrology*, 231-232, 195–206.
586 [https://doi.org/10.1016/s0022-1694\(00\)00194-3](https://doi.org/10.1016/s0022-1694(00)00194-3)

587 18. DeBano, L.F. (2000b). Water repellency in soils: A historical review. *Journal of*
588 *Hydrology*, 231-232, 4-32. [https://doi.org/10.1016/S0022-1694\(00\)00180-3](https://doi.org/10.1016/S0022-1694(00)00180-3)

589 19. Du, Z., Bilbao-Montoya, M.P., Binks, B.P., Dickinson, E., Ettelaie, R., Murray, B.S.
590 (2003). Outstanding Stability of Particle-Stabilized Bubbles. *Langmuir*, 19(8), 3106-
591 3108. <https://doi.org/10.1021/la034042n>

592 20. Dunkerley, D. (2020). Rainfall intensity in geomorphology: Challenges and
593 opportunities. *Progress in Physical Geography: Earth and Environment*, 45(4), 488–513.
594 <https://doi.org/10.1177/0309133320967893>

595 21. Dupuy, J.-L., Fargeon, H., Martin-StPaul, N., Pimont, F., Ruffault, J., Guijarro, M.,
596 Hernando, C., Madrigal, J., & Fernandes, P. (2020). Climate change impact on future
597 wildfire danger and activity in Southern Europe: A Review. *Annals of Forest Science*,
598 77(2). <https://doi.org/10.1007/s13595-020-00933-5>

599 22. Fried, J. S., Torn, M. S., & Mills, E. (2004). The impact of climate change on wildfire
600 severity: A regional forecast for Northern California. *Climatic Change*, 64(1/2), 169–191.
601 <https://doi.org/10.1023/b:clim.0000024667.89579.ed>

602 23. Garoosi, F., Nicole Mellado-Cusichua, A., Shademani, M., & Shakibaeinia, A. (2022).
603 Experimental and numerical investigations of dam break flow over dry and wet beds.
604 *International Journal of Mechanical Sciences*, 215, 106946.
605 <https://doi.org/10.1016/j.ijmecsci.2021.106946>

- 606 24. Goss, M., Swain, D. L., Abatzoglou, J. T., Sarhadi, A., Kolden, C. A., Williams, A. P., &
607 Duffenbaugh, N. S. (2020). Climate change is increasing the likelihood of extreme
608 autumn wildfire conditions across California. *Environmental Research Letters*, *15*(9),
609 094016. <https://doi.org/10.1088/1748-9326/ab83a7>
- 610 25. Halofsky, J. E., Peterson, D. L., & Harvey, B. J. (2020). Changing wildfire, changing
611 forests: The effects of climate change on fire regimes and vegetation in the Pacific
612 Northwest, USA. *Fire Ecology*, *16*(1). <https://doi.org/10.1186/s42408-019-0062-8>
- 613 26. Huffman, E. L., MacDonald, L. H., & Stednick, J. D. (2001). Strength and persistence of
614 fire-induced soil hydrophobicity under ponderosa and Lodgepole Pine, Colorado front
615 range. *Hydrological Processes*, *15*(15), 2877–2892. <https://doi.org/10.1002/hyp.379>
- 616 27. Jin, J., Ooi, C. H., Dao, D. V., & Nguyen, N.-T. (2018). Liquid marble coalescence via
617 vertical collision. *Soft Matter*, *14*(20), 4160–4168. <https://doi.org/10.1039/c8sm00121a>
- 618 28. Kean, J. W., Staley, D. M., & Cannon, S. H. (2011). In situ measurements of post-fire
619 debris flows in Southern California: Comparisons of the timing and magnitude of 24
620 debris-flow events with rainfall and soil moisture conditions. *Journal of Geophysical*
621 *Research*, *116*(F4). <https://doi.org/10.1029/2011jf002005>
- 622 29. Kean, J. W., Staley, D. M., Lancaster, J. T., Rengers, F. K., Swanson, B. J., Coe, J. A.,
623 Hernandez, J. L., Sigman, A. J., Allstadt, K. E., & Lindsay, D. N. (2019). Inundation,
624 flow dynamics, and damage in the 9 January 2018 Montecito Debris-flow event,
625 California, USA: Opportunities and challenges for post-wildfire risk assessment.
626 *Geosphere*, *15*(4), 1140–1163. <https://doi.org/10.1130/ges02048.1>
- 627 30. Lamb, M. P., Scheingross, J. S., Amidon, W. H., Swanson, E., & Limaye, A. (2011). A
628 model for fire-induced sediment yield by dry Ravel in steep landscapes. *Journal of*
629 *Geophysical Research*, *116*(F3). <https://doi.org/10.1029/2010jf001878>

- 630 31. Lee, S. H.-H., & Widjaja, B. (2013). Phase concept for mudflow based on the influence
631 of viscosity. *Soils and Foundations*, 53(1), 77–90.
632 <https://doi.org/10.1016/j.sandf.2012.12.005>
- 633 32. Leelamanie, D.A.L., Karube, J., Yoshida, A. (2008). Characterizing water repellency
634 indices: Contact angle and water drop penetration time of hydrophobized sand. *Soil*
635 *Science & Plant Nutrition*, 54(2), 179-187. <https://doi.org/10.1111/j.1747->
636 [0765.2007.00232.x](https://doi.org/10.1111/j.1747-0765.2007.00232.x)
- 637 33. Lozano, O.M., Salis, M., Ager, A.A., Arca, B., Alcasena, F.J., Monteiro, A.T., Finney,
638 M.A., Del Giudice, L., Scoccimarro, E., & Spano, D. (2017). Assessing climate change
639 impacts on wildfire exposure in Mediterranean areas. *Risk Analysis*, 37, 1898-1916.
640 <https://doi.org/10.1111/risa.12739>
- 641 34. Lugni, C., Brocchini, M., & Faltinsen, O. M. (2006). Wave impact loads: The role of the
642 flip-through. *Physics of Fluids*, 18(12). <https://doi.org/10.1063/1.2399077>
- 643 35. McHale G., and Newton, M.I., (2011). Liquid Marbles: Principles and applications. *Soft*
644 *Matter*, 12, 5473–5481
- 645 36. McHale G., and Newton, M.I., (2015). Liquid Marbles: Topical context within soft
646 matter and recent progress. *Soft Matter*, 13, 2530-2546
- 647 37. Morell, K.D., Alessio, P., Dunne, T. and Keller, E., (2021). Sediment Recruitment and
648 Redistribution in Mountain Channel Networks by Post-Wildfire Debris Flows.
649 *Geophysical Research Letters*, 48(24), p.e2021GL095549.
- 650 38. Movasat, M., & Tomac, I. (2021). Assessment of physical properties of water-repellent
651 soils. *Journal of Geotechnical and Geoenvironmental Engineering*, 147(9).
652 [https://doi.org/10.1061/\(asce\)gt.1943-5606.0002604](https://doi.org/10.1061/(asce)gt.1943-5606.0002604)

- 653 39. Neary, D. G., Ryan, K. C., & DeBano, L. F. (2005). Wildland fire in ecosystems: effects
654 of fire on soils and water. Gen. Tech. Rep. RMRS-GTR-42-vol.4. Ogden, UT: U.S.
655 Department of Agriculture, Forest Service, Rocky Mountain Research Station.
- 656 40. Ng, C. W., Zheng, M., Liu, H., & Poudyal, S. (2022). Effects of bed hydrophobicity on
657 post-fire debris flow entrainment and momentum growth. *Journal of Geophysical*
658 *Research: Earth Surface*, 127(11). <https://doi.org/10.1029/2022jf006783>
- 659 41. Ong, X. Y., Taylor, S. E., & Ramaioli, M. (2021). On the formation of dry granular jets at
660 a liquid surface. *Chemical Engineering Science*, 245, 116958.
661 <https://doi.org/10.1016/j.ces.2021.116958>
- 662 42. Paul, E. L., Atiemo-Obeng, V. A., & Kresta, S. M. (2004). *Handbook of Industrial*
663 *Mixing Science and Practice*. Wiley-Interscience.
- 664 43. Perkins, J. P., Diaz, C., Corbett, S. C., Cerovski-Darriau, C., Stock, J. D., Prancevic, J. P.,
665 Micheli, E., & Jasperse, J. (2022). Multi-stage soil-hydraulic recovery and limited Ravel
666 accumulations following the 2017 Nuns and Tubbs wildfires in Northern California.
667 *Journal of Geophysical Research: Earth Surface*, 127(6).
668 <https://doi.org/10.1029/2022jf006591>
- 669 44. Römkens, M. J. M., Prasad, S. N., & Gerits, J. J. P. (1997). Soil erosion modes of sealing
670 soils: A phenomenological study. *Soil Technology*, 11(1), 31–41.
671 [https://doi.org/10.1016/s0933-3630\(96\)00113-4](https://doi.org/10.1016/s0933-3630(96)00113-4)
- 672 45. Savage, S. M. (1974). Mechanism of fire-induced water repellency in soil. *Soil Science*
673 *Society of America Proceedings*, 38, 652-657
- 674 46. Sheng, L. T., Tai, Y. C., Kuo, C. Y., & Hsiau, S. S. (2013). A two-phase model for dry
675 density-varying granular flows. *Advanced Powder Technology*, 24(1), 132–142.
676 <https://doi.org/10.1016/j.appt.2012.04.001>

- 677 47. Song, D., Chen, X., Zhou, G. G. D., Lu, X., Cheng, G., & Chen, Q. (2021). Impact
678 dynamics of debris flow against rigid obstacle in laboratory experiments. *Engineering*
679 *Geology*, 291, 106211. <https://doi.org/10.1016/j.enggeo.2021.106211>
- 680 48. Suhr, J. L., Jarrett, A. R., & Hoover, J. R. (1984). The effect of soil air entrapment on
681 erosion. *Transactions of the ASAE*, 27(1), 0093–0098.
682 <https://doi.org/10.13031/2013.32742>
- 683 49. Tao, D. (2005). Role of bubble size in flotation of coarse and fine particles—a review.
684 *Separation Science and Technology*, 39(4), 741–760. [https://doi.org/10.1081/ss-](https://doi.org/10.1081/ss-120028444)
685 120028444
- 686 50. Tanaka, Y., Uchida, T., Nagai, H., & Todate, H. (2019). Bench-scale experiments on
687 effects of pipe flow and entrapped air in soil layer on hillslope landslides. *Geosciences*,
688 9(3), 138. <https://doi.org/10.3390/geosciences9030138>
- 689 51. Tessler, N., Wittenberg, L., & Greenbaum N. (2013). Soil water repellency persistence
690 after recurrent forest fires on Mount Carmel, Israel. *International Journal of Wildland*
691 *Fire*, 22, 515-526.
- 692 52. United States Department of Agriculture Forest Service. (2021a). Monument Fire Burned-
693 Area Report. [https://forest.moscowfsl.wsu.edu/BAERTOOLS/baer-db/2500-8/2500-](https://forest.moscowfsl.wsu.edu/BAERTOOLS/baer-db/2500-8/2500-8_Monument_Shasta-Trinity.pdf)
694 8_Monument_Shasta-Trinity.pdf
- 695 53. United States Department of Agriculture Forest Service. (2021b). McCash Fire Burned-Area
696 Report. [https://forest.moscowfsl.wsu.edu/BAERTOOLS/baer-db/2500-8/2500-](https://forest.moscowfsl.wsu.edu/BAERTOOLS/baer-db/2500-8/2500-8_McCash_Six%20Rivers.pdf)
697 8_McCash_Six%20Rivers.pdf
- 698 54. United States Department of Agriculture Forest Service. (2021c). French Fire Burned-Area
699 Report. [https://forest.moscowfsl.wsu.edu/BAERTOOLS/baer-db/2500-8/2500-](https://forest.moscowfsl.wsu.edu/BAERTOOLS/baer-db/2500-8/2500-8_French_Sequoia.pdf)
700 8_French_Sequoia.pdf

- 701 55. Wang, G., Evans, G. M., & Jameson, G. J. (2016). Bubble–particle detachment in a
702 turbulent Vortex I: Experimental. *Minerals Engineering*, 92, 196–207.
703 <https://doi.org/10.1016/j.mineng.2016.03.011>
- 704 56. Wang, A., Hoque, M. M., Evans, G., & Mitra, S. (2022). Determining collision efficiency
705 in multi-bubble-particle systems in presence of turbulence. *Minerals Engineering*, 189,
706 107889. <https://doi.org/10.1016/j.mineng.2022.107889>
- 707 57. Westerling, A. L., Bryant, B. P., Preisler, H. K., Holmes, T. P., Hidalgo, H. G., Das, T.,
708 & Shrestha, S. R. (2011). Climate change and growth scenarios for California wildfire.
709 *Climatic Change*, 109(S1), 445–463. <https://doi.org/10.1007/s10584-011-0329-9>
- 710 58. Westerling, A. L., & Bryant, B. P. (2008). Climate change and wildfire in California.
711 *Climatic Change*, 87(S1), 231–249. <https://doi.org/10.1007/s10584-007-9363-z>
- 712 59. Williams, A. P., Abatzoglou, J. T., Gershunov, A., Guzman-Morales, J., Bishop, D. A.,
713 Balch, J. K., & Lettenmaier, D. P. (2019). Observed impacts of anthropogenic climate
714 change on wildfire in California. *Earth's Future*, 7(8), 892–910.
715 <https://doi.org/10.1029/2019ef001210>
- 716 60. Wotton, B. M., Flannigan, M. D., & Marshall, G. A. (2017). Potential climate change
717 impacts on fire intensity and key wildfire suppression thresholds in Canada.
718 *Environmental Research Letters*, 12(9), 095003. [https://doi.org/10.1088/1748-](https://doi.org/10.1088/1748-9326/aa7e6e)
719 [9326/aa7e6e](https://doi.org/10.1088/1748-9326/aa7e6e)

720

721 **References in Supporting Information:**

- 722 1. Balasubramanian, A. K., Miller, A. C., & Rediniotis, O. K. (2004). Microstructured
723 hydrophobic skin for hydrodynamic drag reduction. *AIAA Journal*, 42(2), 411–414.
724 <https://doi.org/10.2514/1.9104>

- 725 2. Binks, B. P. & Lumsdon, S. O. (2001). Pickering emulsions stabilized by monodisperse
726 latex particles: effects of particle size. *Langmuir*, 17(15), 4540–4547.
727 <https://doi.org/10.1021/la0103822>
- 728 3. Brabcová, Z., Karapantsios, T., Kostoglou, M., Basařová, P., & Matis, K. (2015).
729 Bubble particle collision interaction in flotation systems. *Colloids and Surfaces A:
730 Physicochemical and Engineering Aspects*, 473, 95–103.
731 <https://doi.org/10.1016/j.colsurfa.2014.11.040>
- 732 4. Drzymala, J. (1994). Characterization of materials by Hallimond tube flotation. Part 2:
733 Maximum size of floating particles and contact angle. *International Journal of Mineral
734 Processing*, 42(3–4), 153–167. [https://doi.org/10.1016/0301-7516\(94\)00035-2](https://doi.org/10.1016/0301-7516(94)00035-2)
- 735 5. Eskinlou, A., Chegeni, M. H., Khalesi, M. R., Abdollahy, M., & Huang, Q. (2019).
736 Modeling the bubble loading based on force balance on the particles attached to the
737 bubble. *Colloids and Surfaces A: Physicochemical and Engineering Aspects*, 582,
738 123892. <https://doi.org/10.1016/j.colsurfa.2019.123892>
- 739 6. Fornasiero, D., & Filippov, L. O. (2017). Innovations in the flotation of fine and coarse
740 particles. *Journal of Physics: Conference Series*, 879, 012002.
741 <https://doi.org/10.1088/1742-6596/879/1/012002>
- 742 7. Fielden, M. L., Hayes, R. A., & Ralston, J. (1996). Surface and capillary forces affecting
743 air bubble–particle interactions in aqueous electrolyte. *Langmuir*, 12(15), 3721–3727.
744 <https://doi.org/10.1021/la960145c>
- 745 8. Frith, W. J., Pichot, R., Kirkland, M., & Wolf, B. (2008). Formation, stability, and
746 rheology of particle stabilized emulsions: Influence of multivalent cations. *Industrial &
747 Engineering Chemistry Research*, 47(17), 6434–6444. <https://doi.org/10.1021/ie071629e>

- 748 9. Gai, G., Hadjadj, A., Kudriakov, S., & Thomine, O. (2020). Particles-induced
749 turbulence: A critical review of physical concepts, Numerical Modelings and
750 experimental investigations. *Theoretical and Applied Mechanics Letters*, 10(4), 241–
751 248. <https://doi.org/10.1016/j.taml.2020.01.026>
- 752 10. Gao, Y., Evans, G. M., Wanless, E. J., & Moreno-Atanasio, R. (2014). DEM simulation
753 of single bubble flotation: Implications for the hydrophobic force in particle–bubble
754 interactions. *Advanced Powder Technology*, 25(4), 1177–1184.
755 <https://doi.org/10.1016/j.appt.2014.05.020>
- 756 11. Geraldi, N. R., Dodd, L. E., Xu, B. B., Wells, G. G., Wood, D., Newton, M. I., &
757 McHale, G. (2017). Drag reduction properties of superhydrophobic mesh pipes. *Surface*
758 *Topography: Metrology and Properties*, 5(3), 034001. [https://doi.org/10.1088/2051-](https://doi.org/10.1088/2051-672x/aa793b)
759 [672x/aa793b](https://doi.org/10.1088/2051-672x/aa793b)
- 760 12. Gillies, G., Kappl, M., & Butt, H.-J. (2005). Direct measurements of particle–bubble
761 interactions. *Advances in Colloid and Interface Science*, 114-115, 165–172.
762 <https://doi.org/10.1016/j.cis.2004.08.003>
- 763 13. Haney, B., Chen, D., Cai, L.-H., Weitz, D., & Ramakrishnan, S. (2019). Millimeter-size
764 Pickering emulsions stabilized with Janus microparticles. *Langmuir*, 35(13), 4693–
765 4701. <https://doi.org/10.1021/acs.langmuir.9b00058>
- 766 14. Ishida, N. (2007). Direct measurement of hydrophobic particle–bubble interactions in
767 aqueous solutions by atomic force microscopy: Effect of particle hydrophobicity.
768 *Colloids and Surfaces A: Physicochemical and Engineering Aspects*, 300(3), 293–299.
769 <https://doi.org/10.1016/j.colsurfa.2007.02.003>

- 770 15. Johnson, D. J., Miles, N. J., & Hilal, N. (2006). Quantification of particle–bubble
771 interactions using atomic force microscopy: A Review. *Advances in Colloid and*
772 *Interface Science*, 127(2), 67–81. <https://doi.org/10.1016/j.cis.2006.11.005>
- 773 16. Liu, T. Y., & Schwarz, M. P. (2009). CFD-based modeling of bubble-particle collision
774 efficiency with mobile bubble surface in a turbulent environment. *International Journal*
775 *of Mineral Processing*, 90(1-4), 45–55. <https://doi.org/10.1016/j.minpro.2008.10.004>
- 776 17. Lu, S. (1991). Hydrophobic interaction in flocculation and flotation 3. Role of
777 hydrophobic interaction in particle—bubble attachment. *Colloids and Surfaces*, 57(1),
778 73–81. [https://doi.org/10.1016/0166-6622\(91\)80181-m](https://doi.org/10.1016/0166-6622(91)80181-m)
- 779 18. Maxwell, R., Ata, S., Wanless, E. J., & Moreno-Atanasio, R. (2012). Computer
780 simulations of particle–bubble interactions and particle sliding using discrete element
781 method. *Journal of Colloid and Interface Science*, 381(1), 1–10.
782 <https://doi.org/10.1016/j.jcis.2012.05.021>
- 783 19. Movasat, M., Cruz, A. D., & Tomac, I. (2023). Role of hydrophobic sand particle
784 granularity on water droplet post-impact dynamics. *International Journal of Multiphase*
785 *Flow*, 167, 104529. <https://doi.org/10.1016/j.ijmultiphaseflow.2023.104529>
- 786 20. Nguyen, A. V., Schulze, H. J., & Ralston, J. (1997). Elementary steps in particle—
787 bubble attachment. *International Journal of Mineral Processing*, 51(1-4), 183–195.
788 [https://doi.org/10.1016/s0301-7516\(97\)00030-6](https://doi.org/10.1016/s0301-7516(97)00030-6)
- 789 21. Nguyen, A. V., & Evans, G. M. (2002a). The liquid flow force on a particle in the
790 bubble–particle interaction in flotation. *Journal of Colloid and Interface Science*,
791 246(1), 100–104. <https://doi.org/10.1006/jcis.2001.8010>
- 792 22. Nguyen, A. V., & Evans, G. M. (2002b). Axisymmetric approach of a solid sphere
793 toward a non-deformable planar slip interface in the normal stagnation flow—

- 794 development of global rational approximations for resistance coefficients. *International*
795 *Journal of Multiphase Flow*, 28(8), 1369–1380. [https://doi.org/10.1016/s0301-](https://doi.org/10.1016/s0301-9322(02)00025-3)
796 9322(02)00025-3
- 797 23. Phan, C. M., Nguyen, A. V., Miller, J. D., Evans, G. M., & Jameson, G. J. (2003).
798 Investigations of bubble–particle interactions. *International Journal of Mineral*
799 *Processing*, 72(1-4), 239–254. [https://doi.org/10.1016/s0301-7516\(03\)00102-9](https://doi.org/10.1016/s0301-7516(03)00102-9)
- 800 24. Preuss, M., & Butt, H.-J. (1998). Direct measurement of particle–bubble interactions in
801 aqueous electrolyte: dependence on surfactant. *Langmuir*, 14(12), 3164–3174.
802 <https://doi.org/10.1021/la971349b>
- 803 25. Pyke, B., Fornasiero, D., & Ralston, J. (2003). Bubble particle heterocoagulation under
804 turbulent conditions. *Journal of Colloid and Interface Science*, 265(1), 141–151.
805 [https://doi.org/10.1016/s0021-9797\(03\)00345-x](https://doi.org/10.1016/s0021-9797(03)00345-x)
- 806 26. Ralston, J., & Dukhin, S. S. (1999). The interaction between particles and bubbles.
807 *Colloids and Surfaces A: Physicochemical and Engineering Aspects*, 151(1–2), 3–14.
808 [https://doi.org/10.1016/s0927-7757\(98\)00642-6](https://doi.org/10.1016/s0927-7757(98)00642-6)
- 809 27. Shi, L., Hu, C., Bai, M., & Lv, J. (2019). Molecular dynamics study on drag reduction
810 mechanism of nonwetting surfaces. *Computational Materials Science*, 170, 109127.
811 <https://doi.org/10.1016/j.commatsci.2019.109127>
- 812 28. Schulze, H. J. (1982). Dimensionless number and approximate calculation of the upper
813 particle size of floatability in flotation machines. *International Journal of Mineral*
814 *Processing*, 9(4), 321–328. [https://doi.org/10.1016/0301-7516\(82\)90038-2](https://doi.org/10.1016/0301-7516(82)90038-2)
- 815 29. Schulze, H. J. (1989). Hydrodynamics of bubble-mineral particle collisions. *Mineral*
816 *Processing and Extractive Metallurgy Review*, 5(1-4), 43–76.
817 <https://doi.org/10.1080/08827508908952644>

- 818 30. Sutherland, K. L. (1948). Physical chemistry of flotation. XI. Kinetics of the flotation
819 process. *The Journal of Physical and Colloid Chemistry*, 52(2), 394–425.
820 <https://doi.org/10.1021/j150458a013>
- 821 31. Tao, D. (2005). Role of bubble size in flotation of coarse and fine particles—a review.
822 *Separation Science and Technology*, 39(4), 741–760. [https://doi.org/10.1081/ss-](https://doi.org/10.1081/ss-120028444)
823 [120028444](https://doi.org/10.1081/ss-120028444)
- 824 32. Verrelli, D. I., Koh, P. T. L., & Nguyen, A. V. (2011). Particle–bubble interaction and
825 attachment in flotation. *Chemical Engineering Science*, 66(23), 5910–5921.
826 <https://doi.org/10.1016/j.ces.2011.08.016>
- 827 33. Wang, G., Evans, G. M., & Jameson, G. J. (2016a). Bubble–particle detachment in a
828 turbulent Vortex I: Experimental. *Minerals Engineering*, 92, 196–207.
829 <https://doi.org/10.1016/j.mineng.2016.03.011>
- 830 34. Wang, G., Nguyen, A. V., Mitra, S., Joshi, J. B., Jameson, G. J., & Evans, G. M.
831 (2016b). A review of the mechanisms and models of bubble-particle detachment in
832 froth flotation. *Separation and Purification Technology*, 170, 155–172.
833 <https://doi.org/10.1016/j.seppur.2016.06.041>

834

835